Available online at www.sciencedirect.com

ScienceDirect

Nuclear Physics B 979 (2022) 115763

NUCLEAR PHYSICS B

www.elsevier.com/locate/nuclphysb

New physics in $b \to s\ell\ell$ anomalies and its implications for the complementary neutral current decays

Faisal Munir Bhutta [a], Zhuo-Ran Huang [b,c,*], Cai-Dian Lü [d,e], M. Ali Paracha [f], Wenyu Wang [a]

[a] *Institute of Theoretical Physics, Faculty of Science, Beijing University of Technology, Beijing 100124, China*
[b] *Université Paris-Saclay, CNRS/IN2P3, IJCLab, 91405 Orsay, France*
[c] *Asia Pacific Center for Theoretical Physics, Pohang, 37673, Republic of Korea*
[d] *Institute of High Energy Physics, Chinese Academy of Sciences, Beijing 100049, China*
[e] *School of Physics, University of Chinese Academy of Sciences, Beijing 100049, China*
[f] *Department of Physics, School of Natural Sciences (SNS), National University of Sciences and Technology (NUST), Sector H-12 Islamabad, Pakistan*

Received 27 December 2021; received in revised form 18 February 2022; accepted 29 March 2022
Available online 12 April 2022
Editor: Hong-Jian He

Abstract

We study the Standard Model and the new physics predictions for the lepton-flavour-universality violating (LFUV) ratios in various $b \to s\ell^+\ell^-$ channels with scalar, pseudoscalar, vector, axial-vector, and Λ baryon final states, considering both unpolarized and polarized final state hadrons. In order to formulate physical observables, we use the model independent effective Hamiltonian approach and employ the helicity formalism. We provide the explicit expressions of the helicity amplitudes in terms of the Wilson coefficients and the hadronic form factors by using the same kinematical configuration and polarization conventions for all the decay channels. We perform the numerical analysis with new physics scenarios selected from the recent global fits to $b \to s\ell^+\ell^-$ data, having specific new physics model interpretations. We find that some of the LFUV ratios for these complementary channels in different kinematical regions have high sensitivity to new physics and the future measurements of them in Belle II and LHCb experiments, along with testing new physics/LFUV, can help to distinguish among some of the different new physics possibilities.

* Corresponding author.
E-mail addresses: faisalmunir@bjut.edu.cn (F.M. Bhutta), zhuoran.huang@apctp.org (Z.-R. Huang), lucd@ihep.ac.cn (C.-D. Lü), aliparacha@sns.nust.edu.pk (M. Ali Paracha), wywang@bjut.edu.cn (W. Wang).

https://doi.org/10.1016/j.nuclphysb.2022.115763

Table 1
Experimental values for the LFD observable P_5' in different q^2 bins.

LFD observable	Measured value	Deviation	Collaboration
$\langle P_5' \rangle^{[4.3,\,8.68]}$	$-0.19^{+0.16}_{-0.16} \pm 0.03$	3.7σ	LHCb [3]
$\langle P_5' \rangle^{[4,\,6]}$	$-0.300^{+0.158}_{-0.159} \pm 0.023$	2.8σ	LHCb [4]
$\langle P_5' \rangle^{[6,\,8]}$	$-0.505^{+0.122}_{-0.122} \pm 0.024$	3.0σ	LHCb [4]
$\langle P_5' \rangle^{[4,\,6]}$	$0.26 \pm 0.35 \pm 0.18$	2.7σ	ATLAS [5]
$\langle P_5' \rangle^{[4,\,8]}$	$-0.267^{+0.275}_{-0.269} \pm 0.049$	2.1σ	Belle [6]
$\langle P_5^{\mu'} \rangle^{[4,\,8]}$	$-0.03^{+0.31}_{-0.30} \pm 0.09$	2.6σ	Belle [7]
$\langle P_5' \rangle^{[6,\,8.68]}$	$-0.64^{+0.15}_{-0.19} \pm 0.13$	$\sim 1.0\sigma$	CMS [8]
$\langle P_5' \rangle^{[4,\,6]}$	$-0.439 \pm 0.111 \pm 0.036$	2.5σ	LHCb [9]
$\langle P_5' \rangle^{[6,\,8]}$	$-0.583 \pm 0.090 \pm 0.030$	2.9σ	LHCb [9]

1. Introduction

Flavour-changing neutral-current (FCNC) processes involving $b \to s\ell^+\ell^-$ quark level transitions can play a pivotal role in the indirect searches of physics beyond the Standard Model (SM). These transitions are CKM and loop suppressed within the SM and therefore have high sensitivity to potential new physics (NP) effects. Interestingly, recent experimental data on neutral current decays induced by $b \to s\ell^+\ell^-$ transitions have pointed towards several observables in tension with the SM predictions. Due to this fact, these transitions currently stand among the most promising indications of NP.

The reported observables can be grouped into two sets: $b \to s\mu^+\mu^-$ observables that include only muons, called as lepton-flavour dependent (LFD) observables, and the other known as lepton-flavour-universality violating (LFUV) observables that involve both muons and electrons. The set of LFD observables contains several angular observables, in particular P_5' observable in the $B^0 \to K^{*0}\mu^+\mu^-$ decay [1,2], showing discrepancies from the SM values, which are collected in Table 1. In addition, more LFD observables such as the branching fractions of the $B \to K\mu^+\mu^-$ [10], $B \to K^*\mu^+\mu^-$ [10–12], and $B_s \to \phi\mu^+\mu^-$ [13,14] decays are found to be on the lower side compared to their SM estimates. These LFD observables, while being sensitive to NP [15–19], can not establish the NP case unambiguously because of the involvement of the hadronic uncertainties originating from the different long-distance effects, in particular from form factors, power corrections, and charm resonances [20–25]. Therefore, without having additional data or a complete and reliable calculations of the hadronic uncertainties there remains a possibility to explain the currently observed LFD anomalies with more conservative assumptions on the involved hadronic contributions [26–30].

The second set with LFUV observables includes the ratios of branching fractions involving both $b \to s\mu^+\mu^-$ and $b \to se^+e^-$ transitions. In Table 2, we list the deviations observed by the LHCb collaboration in ratios $R_K \equiv \mathcal{B}(B^+ \to K^+\mu^+\mu^-)/\mathcal{B}(B^+ \to K^+e^+e^-)$, and

Table 2
LHCb predictions for the LFUV ratios in different q^2 bins.

LFUV observable	Measured value		Deviation
$R_K^{[1,6]}$	$0.745^{+0.090}_{-0.074} \pm 0.036$	[35]	2.6σ
$R_K^{[1.1,6]}$	$0.846^{+0.060+0.016}_{-0.054-0.014}$	[36]	2.5σ
$R_K^{[1.1,6]}$	$0.846^{+0.042+0.013}_{-0.039-0.012}$	[37]	3.1σ
$R_{K^*}^{[0.045,1.1]}$	$0.66^{+0.11}_{-0.07} \pm 0.03$	[38]	2.4σ
$R_{K^*}^{[1.1,6]}$	$0.69^{+0.11}_{-0.07} \pm 0.05$	[38]	2.5σ

$R_{K^*} \equiv \mathcal{B}(B^0 \to K^{*0}\mu^+\mu^-)/\mathcal{B}(B^0 \to K^{*0}e^+e^-)$ from their SM expectation of $\simeq 1$ [31,32]. Additionally, we have recent Belle results for R_K [33] and R_{K^*} [34], which are combined together for the charged and neutral decay modes, and are presented in multiple q^2 bins. However, due to large errors, these results are in agreement with both the SM and the LHCb measurements. Moreover, additional LFUV observables, such as $Q_{4,5} = P'^{\mu}_{4,5} - P'^{e}_{4,5}$ [39], have been observed by the Belle collaboration [7]. Furthermore, LHCb has also performed the test of lepton flavour universality (LFU) violation in the baryon decay $\Lambda_b \to pK^-\ell^+\ell^-$ [40], and the decays $B^+ \to K^{*+}\ell^+\ell^-$ and $B^0 \to {K_S}^0\ell^+\ell^-$ [41] which are isospin partners of the formerly tested $B^0 \to K^{*0}\ell^+\ell^-$ and $B^+ \to K^+\ell^+\ell^-$ decays. All the measured central values of the LFUV ratios corresponding to these decays are lower than the SM predictions, which shows a consistent tendency. Contrary to the LFD observables, SM predictions for the LFUV observables R_K and R_{K^*} are theoretically clean as the hadronic uncertainties essentially cancel and therefore they hold the key to unravel NP without ambiguity.

Interestingly, several model independent global fit analyses [42–58] performed with the assumption of LFUV NP present only in the $b \to s\mu^+\mu^-$ sector have pointed out two simple one-dimensional (1D) NP scenarios (S1) $C_{9\mu}^{\rm NP}$ or (S2) $C_{9\mu}^{\rm NP} = -C_{10\mu}^{\rm NP}$, that can provide better fit to all the $b \to s$ data with preferences reaching $\approx 5-6\sigma$ compared to the SM. However, performing the separate fits, it is observed that the inclusion of the more recent R_K and R_{K^*} data has created tensions between the separate fit to LFD and LFUV set in both the scenarios S1 and S2 along with increasing the significance gap between the two LFUV fits of the two scenarios [42,50,53]. These tensions, if not statistical fluctuations, could be indications of NP also present in $b \to se^+e^-$. For instance, in Ref. [53], it is shown that the additional LFUV NP in $b \to se^+e^-$ along with the basic scenarios S1 and S2 leads to a number of new scenarios, which can remove tensions along with improving the overall fit to all data. Another complementary approach proposed in [59], before the latest R_K and R_{K^*} measurement, showed that several scenarios with both LFU and LFUV NP contributions to the Wilson coefficients (WC), $C_{9\ell}^{\rm NP}$ and $C_{10\ell}^{\rm NP}$ can improve the agreement with the overall data. After the latest R_K and R_{K^*} data, more updated global fit analyses [42,50], have again pointed out various NP scenarios with enhanced significance, and an improved preference for the NP scenarios with right-handed currents (RHC) have been observed to emerge. Furthermore, a better description of data can also be obtained by increasing the degrees of freedom, i.e., 2D fits, along with the assumptions such as NP affects only muons.

As there is no unique solution and many new scenarios are piling up due to the recently emerging NP patterns in global fit analyses, it is particularly important to discriminate between

different possible scenarios and to devise methods to further confirm or constrain patterns of NP [60,61]. One way is to consider the complementary channels induced by the same quark level $b \to s\ell^+\ell^-$ transitions, and analyze the implications of the different NP scenarios for the theoretically clean LFUV ratios in different kinematical regions. The list of decay channels induced by the $b \to s\ell^+\ell^-$ transition is long, and the LFUV ratios in a number of decay channels have been studied [62–65] based on the previous data. In the present study, we consider the most recent experimental results and restrict to seven exclusive channels $M_{in} \to M_f \ell^+\ell^-$, with $M_{in} = B, B_s, \Lambda_b$ and $M_f = f_0, K_0^*, K, K^*, \phi, K_1, \Lambda$. We study these channels in the model independent effective Hamiltonian approach by employing the helicity formalism. The theoretical analysis of LFUV observables in complementary hadronic decays, along with providing additional tests of LFU, similar to being performed in R_K and R_{K^*}, can help to distinguish and further strengthen some of the emerging NP patterns in the global fit analyses, before going on to build the accurate NP models accommodating the B decay anomalies [66–68].

The paper is organized as follows. In section 2, we describe the effective Hamiltonian and the decay amplitude for $b \to s\ell^+\ell^-$ transitions. In section 3, we consider the helicity formalism and work out the explicit expressions of the helicity amplitudes for the considered decays. In section 4, we construct LFUV observables. Section 5, is devoted to numerical analysis, where we also present our choice of the NP scenarios from different global fit analyses. The results are summarized in section 6.

2. Effective Hamiltonian and decay amplitude

The effective weak Hamiltonian for $b \to s\ell^+\ell^-$ transition is given by

$$\mathcal{H}_{\rm eff} = -\frac{4G_F}{\sqrt{2}} V_{tb}V_{ts}^* \Bigg[\sum_{i=1}^{6} C_i O_i + \sum_{i=7}^{8} \left(C_i O_i + C_{i'} O_{i'} \right) + \sum_{i=9,10} \left((C_i + C_{i\ell}^{\rm NP}) O_i + C_{i'\ell}^{\rm NP} O_{i'} \right) \Bigg], \tag{1}$$

where we have neglected the doubly Cabibbo suppressed contribution ($\propto V_{ub}V_{us}^*$), and G_F is the Fermi coupling constant. The operators $O_{i\leq 6}$ are the same as the $P_{1,2}^c$, $P_{3,\ldots,6}$, given in Ref. [69], and the others are

$$\begin{aligned}
O_7 &= \frac{e}{16\pi^2} m_b \left(\bar{s}\sigma_{\mu\nu} P_R b\right) F^{\mu\nu}, & O_{7'} &= \frac{e}{16\pi^2} m_b \left(\bar{s}\sigma_{\mu\nu} P_L b\right) F^{\mu\nu},\\
O_8 &= \frac{g_s}{16\pi^2} m_b \left(\bar{s}\sigma_{\mu\nu} T^a P_R b\right) G^{\mu\nu a}, & O_{8'} &= \frac{g_s}{16\pi^2} m_b \left(\bar{s}\sigma_{\mu\nu} T^a P_L b\right) G^{\mu\nu a},\\
O_9 &= \frac{e^2}{16\pi^2} (\bar{s}\gamma_\mu P_L b)(\bar{l}\gamma^\mu l), & O_{9'} &= \frac{e^2}{16\pi^2} (\bar{s}\gamma_\mu P_R b)(\bar{l}\gamma^\mu l),\\
O_{10} &= \frac{e^2}{16\pi^2} (\bar{s}\gamma_\mu P_L b)(\bar{l}\gamma^\mu \gamma_5 l), & O_{10'} &= \frac{e^2}{16\pi^2} (\bar{s}\gamma_\mu P_R b)(\bar{l}\gamma^\mu \gamma_5 l),
\end{aligned} \tag{2}$$

where e (g_s) is the electromagnetic (strong) coupling constant, and m_b represents the running b-quark mass in the $\overline{\rm MS}$ scheme.

Within the SM, major role in $b \to s\ell^+\ell^-$ transition, is played by operators $O_{7,9,10}$, whereas contributions of primed dipole operators $O_{7',8'}$ are suppressed by m_s/m_b, and therefore we neglect them. Furthermore, the factorizable contributions from current-current, QCD penguins and

Table 3
The SM Wilson coefficients C_i^μ up to NNLL accuracy given at the scale $\mu \sim m_b$.

C_1	C_2	C_3	C_4	C_5	C_6	C_7	C_8	C_9	C_{10}
−0.294	1.017	−0.0059	−0.087	0.0004	0.0011	−0.324	−0.176	4.114	−4.193

chromomagnetic dipole operators $O_{1-6,8}$ can be absorbed into the effective Wilson coefficients $C_7^{\rm eff}(q^2)$ and $C_9^{\rm eff}(q^2)$ [69–74]. The explicit expressions of these Wilson coefficients, which we used, are presented in appendix A. It is important to mention that, in Eq. (1), we have considered NP contributions only in $O_{9^{(\prime)}}$ and $O_{10^{(\prime)}}$ operators because the emerging viable NP solutions from the global fits of all the $b \to s$ data, which we consider in our study, are only in the form of vector and axial-vector operators. The numerical values of Wilson coefficients at $\mu \sim m_b$ in the SM are presented in Table 3.

Using the effective Hamiltonian given in Eq. (1), the decay amplitude for the process $M_{in} \to M_f \ell^+\ell^-$, including the SM and the NP contributions, can be written as[1]

$$\mathcal{M}\left(M_{in} \to M_f \ell^+\ell^-\right) = \frac{G_F \alpha}{2\sqrt{2}\pi} V_{tb} V_{ts}^* \Big\{ T_\mu^{1,M_f} (\bar{\ell}\gamma^\mu \ell) + T_\mu^{2,M_f} (\bar{\ell}\gamma^\mu \gamma_5 \ell) \Big\}, \tag{3}$$

where

$$\begin{aligned} T_\mu^{1,M_f} &= (C_9^{\rm eff} + C_{9\ell}^{\rm NP}) \Big\langle M_f(k)|\bar{s}\gamma_\mu(1-\gamma_5)b|M_{in}(p)\Big\rangle \\ &+ C_{9'\ell}^{\rm NP} \Big\langle M_f(k)|\bar{s}\gamma_\mu(1+\gamma_5)b|M_{in}(p)\Big\rangle \\ &- \frac{2m_b}{q^2} C_7^{\rm eff} \Big\langle M_f(k)|\bar{s} i\sigma_{\mu\nu} q^\nu (1+\gamma_5)b|M_{in}(p)\Big\rangle, \end{aligned} \tag{4}$$

$$\begin{aligned} T_\mu^{2,M_f} &= (C_{10} + C_{10\ell}^{\rm NP}) \Big\langle M_f(k)|\bar{s}\gamma_\mu(1-\gamma_5)b|M_{in}(p)\Big\rangle \\ &+ C_{10'\ell}^{\rm NP} \Big\langle M_f(k)|\bar{s}\gamma_\mu(1+\gamma_5)b|M_{in}(p)\Big\rangle. \end{aligned} \tag{5}$$

To calculate T_μ^{i,M_f} $(i = 1, 2)$, one requires the involved hadronic matrix elements which can be parameterized in terms of the transition form factors. As we consider various decay channels with $M_{in} = B, B_s, \Lambda_b$ and $M_f = f_0, K_0^*, K, K^*, \phi, K_1, \Lambda$, we give the hadronic matrix elements, in terms of the transition form factors, for each case in appendix B. The form factors, for the decay $B_s \to f_0(980)\ell^+\ell^-$, and $B \to K_0^*(1430)\ell^+\ell^-$ can be calculated using the light cone QCD sum rule approach [75], and three-point QCD sum rules [76]. For $B \to K$ transition form factors, light cone sum rules (LCSR) predictions can be extrapolated at $q^2 \leq 8$ GeV^2 to the whole kinematical region by applying z-series expansion [77]. The simplified series expansion for $B \to P$ form factors has been adopted which was originally proposed in [78]. For the decays $B \to K^*\ell^+\ell^-$ and $B_s \to \phi\ell^+\ell^-$, we use the series expansion fits to LCSR and lattice form factors [79]. The transition form factors in terms of rapidly converging series parameter can be expressed as [79] $F_i(q^2) = P_i(q^2) \sum_k \alpha_k^i [z'(q^2) - z'(0)]^k$, where $P_i(q^2) = \frac{1}{(1-q^2/m_{R,i}^2)}$ is simple pole representing

[1] We neglect the non-factorizable contributions such as the non-perturbative charm-loop corrections which are not the expected sources of the deviations in $R_{K^{(*)}}$ [20,24].

the first resonance in the spectrum. For $B \to K_1(1270, 1400)\ell^+\ell^-$ decay, the physical states $K_1(1270)$ and $K_1(1400)$ are mixed states of K_{1A} and K_{1B} with mixing angle θ_{K_1} defined as

$$|K_1(1270)\rangle = |K_{1A}\rangle \sin\theta_{K_1} + |K_{1B}\rangle \cos\theta_{K_1}\,, \tag{6}$$

$$|K_1(1400)\rangle = |K_{1A}\rangle \cos\theta_{K_1} - |K_{1B}\rangle \sin\theta_{K_1}\,. \tag{7}$$

The corresponding mixing relations among different matrix elements and for the form factors are explicitly given in [64,80–82]. For numerical analysis, we use the light-cone QCD sum rule form factors [80]. For the $\Lambda_b \to \Lambda\ell^+\ell^-$ decay, we use the lattice QCD results of the form factors for whole q^2 range [83]. The form factors used in [83] are related to our notation of the form factors as $f^V_{t,0,\perp} = f_{0,+,\perp}$, $f^A_{t,0,\perp} = g_{0,+,\perp}$, $f^T_{0,\perp} = h_{+,\perp}$, and $f^{T_5}_{0,\perp} = \tilde{h}_{+,\perp}$.

3. Helicity formalism and helicity amplitudes

The decay amplitudes can be expressed in terms of helicity basis as described in [84], and references therein. The orthonormality and completeness properties of helicity basis $\varepsilon^\alpha(n = t, +, -, 0)$, with three spin 1 components orthogonal to momentum transfer i.e., $q\cdot\varepsilon(\pm) = q\cdot\varepsilon = 0$, can be expressed as follows

$$\varepsilon^{*\alpha}(n)\varepsilon_\alpha(l) = g_{nl}, \qquad \sum_{n,l=t,+,-,0} \varepsilon^{*\alpha}(n)\varepsilon^\beta(l) g_{nl} = g^{\alpha\beta}, \tag{8}$$

with $g_{nl} = \mathrm{diag}(+,-,-,-)$. Using the completeness property given in Eq. (8), the contraction of leptonic tensors $L^{(k)\alpha\beta}$ and hadronic tensors $H^{ij}_{\alpha\beta} = T^{i,M_f}_\alpha \overline{T}^{j,M_f}_\beta$ $(i, j = 1, 2)$, can be written as

$$L^{(k)\alpha\beta} H^{ij}_{\alpha\beta} = \sum_{n,n',l,l'} L^{(k)}_{nl}\, g_{nn'} g_{ll'} H^{ij}_{n'l'}, \tag{9}$$

where the leptonic and hadronic tensors are expressed in the helicity basis as follows

$$L^{(k)}_{nl} = \varepsilon^\alpha(n)\varepsilon^{*\beta}(l) L^{(k)}_{\alpha\beta}, \qquad H^{ij}_{nl} = \varepsilon^{*\alpha}(n)\varepsilon^\beta(l) H^{ij}_{\alpha\beta}. \tag{10}$$

Both leptonic and hadronic tensors given in Eq. (10), will be evaluated in two different frame of references. The lepton tensor $L^{(k)}_{nl}$ will be evaluated in $l\bar{l}$ CM frame. However the hadron tensor H^{ij}_{nl} will be evaluated in the rest frame of decaying hadron.

3.1. Helicity amplitudes for $M_{in} \to S\ell^+\ell^-$ decays

$$H^{ij}_{nl} = \left(\varepsilon^{*\alpha}(n) T^{i,S}_\alpha\right) \cdot \overline{\left(\varepsilon^{*\beta}(l) T^{j,S}_\beta\right)} \equiv H^{i,S}_n \overline{H}^{j,S}_l, \tag{11}$$

where, for $M_{in} = B_s$, and $S = f_0(980)$, explicit helicity amplitudes are obtained as

$$H^{1,f_0}_t = i\frac{m^2_{B_s} - m^2_{f_0}}{\sqrt{q^2}}(C^{\rm eff}_9 + C^{\rm NP}_{9\ell} - C^{\rm NP}_{9'\ell}) f^{f_0}_0(q^2),$$

$$H^{2,f_0}_t = i\frac{m^2_{B_s} - m^2_{f_0}}{\sqrt{q^2}}(C_{10} + C^{\rm NP}_{10\ell} - C^{\rm NP}_{10'\ell}) f^{f_0}_0(q^2),$$

$$H^{i,f_0}_\pm = 0,$$

$$H_0^{1,f_0} = i\sqrt{\frac{\lambda}{q^2}}\Big[(C_9^{\rm eff} + C_{9\ell}^{\rm NP} - C_{9'\ell}^{\rm NP}) f_+^{f_0}(q^2) + \frac{2m_b}{m_{B_s} + m_{f_0}} C_7^{\rm eff} f_T^{f_0}(q^2)\Big],$$
$$H_0^{2,f_0} = i\sqrt{\frac{\lambda}{q^2}}\Big[(C_{10} + C_{10\ell}^{\rm NP} - C_{10'\ell}^{\rm NP}) f_+^{f_0}(q^2)\Big], \tag{12}$$

similarly, for $M_{in} = B$, and $S = K_0^*(1430)$,

$$H_t^{1,K_0^*} = i(C_9^{\rm eff} + C_{9\ell}^{\rm NP} - C_{9'\ell}^{\rm NP})\Big[\frac{m_B^2 - m_{K_0^*}^2}{\sqrt{q^2}} f_+^{K_0^*}(q^2) + \sqrt{q^2} f_-^{K_0^*}(q^2)\Big],$$
$$H_t^{2,K_0^*} = i(C_{10} + C_{10\ell}^{\rm NP} - C_{10'\ell}^{\rm NP})\Big[\frac{m_B^2 - m_{K_0^*}^2}{\sqrt{q^2}} f_+^{K_0^*}(q^2) + \sqrt{q^2} f_-^{K_0^*}(q^2)\Big],$$
$$H_\pm^{i,K_0^*} = 0,$$
$$H_0^{1,K_0^*} = i\sqrt{\frac{\lambda}{q^2}}\Big[(C_9^{\rm eff} + C_{9\ell}^{\rm NP} - C_{9'\ell}^{\rm NP}) f_+^{K_0^*}(q^2) + \frac{2m_b}{m_B + m_{K_0^*}} C_7^{\rm eff} f_T^{K_0^*}(q^2)\Big],$$
$$H_0^{2,K_0^*} = i\sqrt{\frac{\lambda}{q^2}}\Big[(C_{10} + C_{10\ell}^{\rm NP} - C_{10'\ell}^{\rm NP}) f_+^{K_0^*}(q^2)\Big]. \tag{13}$$

Here $\lambda \equiv \lambda(m_{B_s(B)}^2, m_{f_0(K_0^*)}^2, q^2)$.

3.2. Helicity amplitudes for $M_{in} \to P\ell^+\ell^-$ decays

$$H_{nl}^{ij} = \big(\varepsilon^{*\alpha}(n) T_\alpha^{i,P}\big) \cdot \big(\overline{\varepsilon^{*\beta}(l) T_\beta^{j,P}}\big) \equiv H_n^{i,P}\, \overline{H}_l^{\,j,P}, \tag{14}$$

where, for $M_{in} = B$, and $P = K$, explicit helicity amplitudes are calculated as

$$H_t^{1,K} = \frac{m_B^2 - m_K^2}{\sqrt{q^2}}(C_9^{\rm eff} + C_{9\ell}^{\rm NP} + C_{9'\ell}^{\rm NP}) f_0^K(q^2),$$
$$H_t^{2,K} = \frac{m_B^2 - m_K^2}{\sqrt{q^2}}(C_{10} + C_{10\ell}^{\rm NP} + C_{10'\ell}^{\rm NP}) f_0^K(q^2),$$
$$H_\pm^{i,K} = 0,$$
$$H_0^{1,K} = \sqrt{\frac{\lambda}{q^2}}\Big[(C_9^{\rm eff} + C_{9\ell}^{\rm NP} + C_{9'\ell}^{\rm NP}) f_+^K(q^2) + \frac{2m_b}{m_B + m_K} C_7^{\rm eff} f_T^K(q^2)\Big],$$
$$H_0^{2,K} = \sqrt{\frac{\lambda}{q^2}}\Big[(C_{10} + C_{10\ell}^{\rm NP} + C_{10'\ell}^{\rm NP}) f_+^K(q^2)\Big]. \tag{15}$$

Here $\lambda \equiv \lambda(m_B^2, m_K^2, q^2)$.

3.3. Helicity amplitudes for $M_{in} \to V\ell^+\ell^-$ decays

$$\begin{aligned} H_{nl}^{ij} &= \big(\varepsilon^{*\alpha}(n) T_\alpha^{i,V}\big) \cdot \big(\overline{\varepsilon^{*\beta}(l) T_\beta^{j,V}}\big) \\ &= \big(\varepsilon^{*\alpha}(n)\overline{\epsilon}^{*\mu}(r) T_{\alpha,\mu}^{i,V}\big) \cdot \big(\overline{\varepsilon^{*\beta}(l)\overline{\epsilon}^{*\nu}(s) T_{\beta,\nu}^{j,V}}\big)\delta_{rs} \equiv H_n^{i,V}\, \overline{H}_l^{\,j,V}, \end{aligned} \tag{16}$$

where, from angular momentum conservation, $r = n$ and $s = l$ for $n, l = \pm, 0$ and $r, s = 0$ for $n, l = t$. The explicit helicity amplitudes for $M_{in} = B(B_s)$, and $V = K^*(\phi)$, are derived in terms of the Wilson coefficients and the form factors as[2]

$$
\begin{aligned}
H_t^{1,K^*(\phi)} &= -i\sqrt{\frac{\lambda}{q^2}}(C_9^{\rm eff} + C_{9\ell}^{\rm NP} - C_{9'\ell}^{\rm NP})A_0^{K^*(\phi)},\\
H_t^{2,K^*(\phi)} &= -i\sqrt{\frac{\lambda}{q^2}}(C_{10} + C_{10\ell}^{\rm NP} - C_{10'\ell}^{\rm NP})A_0^{K^*(\phi)},\\
H_\pm^{1,K^*(\phi)} &= -i\left(m_{B(B_s)}^2 - m_{K^*(\phi)}^2\right)\Big[(C_9^{\rm eff} + C_{9\ell}^{\rm NP} - C_{9'\ell}^{\rm NP})\frac{A_1^{K^*(\phi)}}{\left(m_{B(B_s)} - m_{K^*(\phi)}\right)}\\
&\quad + \frac{2m_b}{q^2}C_7^{\rm eff}T_2^{K^*(\phi)}\Big] \pm i\sqrt{\lambda}\Big[(C_9^{\rm eff} + C_{9\ell}^{\rm NP} + C_{9'\ell}^{\rm NP})\frac{V^{K^*(\phi)}}{\left(m_{B(B_s)} + m_{K^*(\phi)}\right)}\\
&\quad + \frac{2m_b}{q^2}C_7^{\rm eff}T_1^{K^*(\phi)}\Big],\\
H_\pm^{2,K^*(\phi)} &= -i(C_{10} + C_{10\ell}^{\rm NP} - C_{10'\ell}^{\rm NP})\left(m_{B(B_s)} + m_{K^*(\phi)}\right)A_1^{K^*(\phi)}\\
&\quad \pm i\sqrt{\lambda}(C_{10} + C_{10\ell}^{\rm NP} + C_{10'\ell}^{\rm NP})\frac{V^{K^*(\phi)}}{\left(m_{B(B_s)} + m_{K^*(\phi)}\right)},\\
H_0^{1,K^*(\phi)} &= -\frac{8im_{B(B_s)}m_{K^*(\phi)}}{\sqrt{q^2}}\left[(C_9^{\rm eff} + C_{9\ell}^{\rm NP} - C_{9'\ell}^{\rm NP})A_{12}^{K^*(\phi)} + m_b C_7^{\rm eff}\frac{T_{23}^{K^*(\phi)}}{m_{B(B_s)} + m_{K^*(\phi)}}\right],\\
H_0^{2,K^*(\phi)} &= -\frac{8im_{B(B_s)}m_{K^*(\phi)}}{\sqrt{q^2}}\left[(C_{10} + C_{10\ell}^{\rm NP} - C_{10'\ell}^{\rm NP})A_{12}^{K^*(\phi)}\right].
\end{aligned}
\tag{17}
$$

Here $\lambda \equiv \lambda(m_{B(B_s)}^2, m_{K^*(\phi)}^2, q^2)$.

3.4. Helicity amplitudes for $M_{in} \to A\ell^+\ell^-$ decays

$$
\begin{aligned}
H_{nl}^{ij} &= \left(\varepsilon^{*\alpha}(n)T_\alpha^{i,A}\right)\cdot\left(\overline{\varepsilon^{*\beta}(l)T_\beta^{j,A}}\right)\\
&= \left(\varepsilon^{*\alpha}(n)\overline{\epsilon}^{*\mu}(r)T_{\alpha,\mu}^{i,A}\right)\cdot\left(\overline{\varepsilon^{*\beta}(l)\overline{\epsilon}^{*\nu}(s)T_{\beta,\nu}^{j,A}}\right)\delta_{rs} \equiv H_n^{i,A}\,\overline{H}_l^{j,A},
\end{aligned}
\tag{18}
$$

where, from angular momentum conservation, $r = n$ and $s = l$ for $n, l = \pm, 0$ and $r, s = 0$ for $n, l = t$. The explicit helicity amplitudes for $M_{in} = B$, and $A = K_1$, are given as

$$
\begin{aligned}
H_t^{1,K_1} &= -\sqrt{\frac{\lambda}{q^2}}(C_9^{\rm eff} + C_{9\ell}^{\rm NP} + C_{9'\ell}^{\rm NP})V_0^{K_1},\\
H_t^{2,K_1} &= -\sqrt{\frac{\lambda}{q^2}}(C_{10} + C_{10\ell}^{\rm NP} + C_{10'\ell}^{\rm NP})V_0^{K_1},
\end{aligned}
$$

[2] With the different conventions used in [85,86], similar expressions of the helicity amplitudes are obtained for $B \to K^*$ channel by employing the more sophisticated generalized helicity amplitude formalism.

Table 4
The possible helicity configurations for $\Lambda_b \to \Lambda \ell^+ \ell^-$ decay.

s_{Λ_b}	s_Λ	$\lambda_{j_{\rm eff}}$
$+\frac{1}{2}$	$-\frac{1}{2}$	$0(t)$
$-\frac{1}{2}$	$+\frac{1}{2}$	$0(t)$
$+\frac{1}{2}$	$+\frac{1}{2}$	1
$-\frac{1}{2}$	$-\frac{1}{2}$	-1

$$
\begin{aligned}
H_{\pm}^{1,K_1} &= -\left(m_B^2 - m_{K_1}^2\right)\left[(C_9^{\rm eff} + C_{9\ell}^{\rm NP} + C_{9'\ell}^{\rm NP})\frac{V_1^{K_1}}{m_B - m_{K_1}} + \frac{2m_b}{q^2}C_7^{\rm eff}T_2^{K_1}\right] \\
&\quad \pm \sqrt{\lambda}\left[(C_9^{\rm eff} + C_{9\ell}^{\rm NP} - C_{9'\ell}^{\rm NP})\frac{A^{K_1}}{m_B + m_{K_1}} + \frac{2m_b}{q^2}C_7^{\rm eff}T_1^{K_1}\right], \\
H_{\pm}^{2,K_1} &= -(C_{10} + C_{10\ell}^{\rm NP} + C_{10'\ell}^{\rm NP})\left(m_B + m_{K_1}\right)V_1^{K_1} \pm \sqrt{\lambda}(C_{10} + C_{10\ell}^{\rm NP} - C_{10'\ell}^{\rm NP})\frac{A^{K_1}}{m_B + m_{K_1}}, \\
H_0^{1,K_1} &= -\frac{1}{2m_{K_1}\sqrt{q^2}}\Bigg[(C_9^{\rm eff} + C_{9\ell}^{\rm NP} + C_{9'\ell}^{\rm NP})\Big\{(m_B^2 - m_{K_1}^2 - q^2)\left(m_B + m_{K_1}\right)V_1^{K_1} \\
&\quad - \frac{\lambda}{m_B + m_{K_1}}V_2^{K_1}\Big\} + 2m_b C_7^{\rm eff}\Big\{(m_B^2 + 3m_{K_1}^2 - q^2)T_2^{K_1} - \frac{\lambda}{m_B^2 - m_{K_1}^2}T_3^{K_1}\Big\}\Bigg], \\
H_0^{2,K_1} &= -\frac{1}{2m_{K_1}\sqrt{q^2}}(C_{10} + C_{10\ell}^{\rm NP} + C_{10'\ell}^{\rm NP})\Bigg[(m_B^2 - m_{K_1}^2 - q^2)\left(m_B + m_{K_1}\right)V_1^{K_1} \\
&\quad - \frac{\lambda}{m_B + m_{K_1}}V_2^{K_1}\Bigg].
\end{aligned} \tag{19}
$$

Here $\lambda \equiv \lambda(m_B^2, m_{K_1}^2, q^2)$.

3.5. Helicity amplitudes for $\Lambda_b \to \Lambda \ell^+ \ell^-$ decay

$$
\begin{aligned}
H_{nl}^{ij} &= \sum_{s_{\Lambda_b}, s_\Lambda}\left(\varepsilon^{*\alpha}(n)T_\alpha^i(s_{\Lambda_b}, s_\Lambda)\right)\cdot\overline{\left(\varepsilon^{*\beta}(l)T_\beta^j(s_{\Lambda_b}, s_\Lambda)\right)} \\
&\equiv \sum_{s_{\Lambda_b}, s_\Lambda} H_n^i(s_{\Lambda_b}, s_\Lambda)\,\overline{H}_l^{\,j}(s_{\Lambda_b}, s_\Lambda).
\end{aligned} \tag{20}
$$

The helicity s_{Λ_b} of the parent baryon is fixed by angular momentum conservation relation, $s_{\Lambda_b} = -s_\Lambda + \lambda_{j_{\rm eff}}$. The possible helicity configurations are shown in Table 4. Using the explicit results of the spinor matrix elements for different combinations of spin orientations, represented in appendix E, we work out the expressions of the non-vanishing helicity amplitudes

$$
\begin{aligned}
H_t^1(\pm 1/2,\mp 1/2) &= \mp\frac{m_{\Lambda_b}-m_\Lambda}{\sqrt{q^2}}\sqrt{s_+}(C_9^{\rm eff}+C_{9\ell}^{\rm NP}+C_{9'\ell}^{\rm NP})f_t^V \\
&\quad -\frac{m_{\Lambda_b}+m_\Lambda}{\sqrt{q^2}}\sqrt{s_-}(C_9^{\rm eff}+C_{9\ell}^{\rm NP}-C_{9'\ell}^{\rm NP})f_t^A, \\
H_t^2(\pm 1/2,\mp 1/2) &= \mp\frac{m_{\Lambda_b}-m_\Lambda}{\sqrt{q^2}}\sqrt{s_+}(C_{10}+C_{10\ell}^{\rm NP}+C_{10'\ell}^{\rm NP})f_t^V \\
&\quad -\frac{m_{\Lambda_b}+m_\Lambda}{\sqrt{q^2}}\sqrt{s_-}(C_{10}+C_{10\ell}^{\rm NP}-C_{10'\ell}^{\rm NP})f_t^A, \\
H_\pm^1(\pm 1/2,\pm 1/2) &= \pm\sqrt{2s_-}\Big[(C_9^{\rm eff}+C_{9\ell}^{\rm NP}+C_{9'\ell}^{\rm NP})f_\perp^V+\frac{2m_b}{q^2}C_7^{\rm eff}(m_{\Lambda_b}+m_\Lambda)f_\perp^T\Big] \\
&\quad -\sqrt{2s_+}\Big[(C_9^{\rm eff}+C_{9\ell}^{\rm NP}-C_{9'\ell}^{\rm NP})f_\perp^A+\frac{2m_b}{q^2}C_7^{\rm eff}(m_{\Lambda_b}-m_\Lambda)f_\perp^{T_5}\Big], \\
H_\pm^2(\pm 1/2,\pm 1/2) &= \pm\sqrt{2s_-}(C_{10}+C_{10\ell}^{\rm NP}+C_{10'\ell}^{\rm NP})f_\perp^V-\sqrt{2s_+}(C_{10}+C_{10\ell}^{\rm NP}-C_{10'\ell}^{\rm NP})f_\perp^A, \\
H_0^1(\pm 1/2,\mp 1/2) &= \mp\sqrt{\frac{s_-}{q^2}}\Big[(C_9^{\rm eff}+C_{9\ell}^{\rm NP}+C_{9'\ell}^{\rm NP})(m_{\Lambda_b}+m_\Lambda)f_0^V+2m_bC_7^{\rm eff}f_0^T\Big] \\
&\quad -\sqrt{\frac{s_+}{q^2}}\Big[(C_9^{\rm eff}+C_{9\ell}^{\rm NP}-C_{9'\ell}^{\rm NP})(m_{\Lambda_b}-m_\Lambda)f_0^A+2m_bC_7^{\rm eff}f_0^{T_5}\Big], \\
H_0^2(\pm 1/2,\mp 1/2) &= \mp\sqrt{\frac{s_-}{q^2}}(C_{10}+C_{10\ell}^{\rm NP}+C_{10'\ell}^{\rm NP})(m_{\Lambda_b}+m_\Lambda)f_0^V \\
&\quad -\sqrt{\frac{s_+}{q^2}}(C_{10}+C_{10\ell}^{\rm NP}-C_{10'\ell}^{\rm NP})(m_{\Lambda_b}-m_\Lambda)f_0^A. \qquad (21)
\end{aligned}
$$

It is important here to mention that the expressions of the helicity amplitudes correspond to intermediate results and depend upon the kinematics and polarization vectors convention. For the $\Lambda_b \to \Lambda\ell^+\ell^-$ decay, our conventions are consistent with that used in Ref. [87]. However, the final decay observables remain same and are independent of the conventions used.

4. Formulation of physical observables

The differential decay rate in terms of helicity amplitudes for $M_{in} \to M_f\ell^+\ell^-$ transitions, with $M_{in} = B, B_s$ and $M_f = f_0, K_0^*, K, K^*, \phi, K_1$, can be expressed as [84]

$$
\begin{aligned}
\frac{d\Gamma\left(M_{in}\to M_f\ell^+\ell^-\right)}{dq^2} &= \frac{G_F^2\alpha^2|V_{tb}V_{ts}^*|^2q^2\sqrt{\lambda}\beta_l}{3.2^9m_{in}^3\pi^5}\Bigg[\frac{2m_\ell^2}{q^2}3\mathcal{R}e\left(H_t^{2,M_f}\overline{H}_t^{2,M_f}\right) \\
&\quad +\left(1+\frac{2m_\ell^2}{q^2}\right)\left[H^{1,M_f^T}\overline{H}^{1,M_f^T}+\mathcal{R}e\left(H_0^{1,M_f}\overline{H}_0^{1,M_f}\right)\right] \\
&\quad +\left(1-\frac{4m_\ell^2}{q^2}\right)\left[H^{2,M_f^T}\overline{H}^{2,M_f^T}+\mathcal{R}e\left(H_0^{2,M_f}\overline{H}_0^{2,M_f}\right)\right]\Bigg], \qquad (22)
\end{aligned}
$$

where

$$
H^{i,M_f^T}\overline{H}^{i,M_f^T} \equiv \mathcal{R}e\left(H_+^{i,M_f}\overline{H}_+^{i,M_f}\right)+\mathcal{R}e\left(H_-^{i,M_f}\overline{H}_-^{i,M_f}\right). \qquad (23)
$$

When the final state (M_f), is a vector or axial-vector, the longitudinal and transverse polarizations can be separated and labelled as L and T, respectively. The corresponding decay rates are written as

$$\frac{d\Gamma(M_{in}\to M_f^L\ell^+\ell^-)}{dq^2} = \frac{G_F^2\alpha^2|V_{tb}V_{ts}^*|^2q^2\sqrt{\lambda}\beta_l}{3.2^9m_{in}^3\pi^5}\Bigg[\frac{2m_\ell^2}{q^2}3\mathcal{R}e\left(H_t^{2,M_f}\overline{H}_t^{2,M_f}\right) + \left(1+\frac{2m_\ell^2}{q^2}\right)\mathcal{R}e\left(H_0^{1,M_f}\overline{H}_0^{1,M_f}\right) + \left(1-\frac{4m_\ell^2}{q^2}\right)\mathcal{R}e\left(H_0^{2,M_f}\overline{H}_0^{2,M_f}\right)\Bigg], \tag{24}$$

$$\frac{d\Gamma(M_{in}\to M_f^T\ell^+\ell^-)}{dq^2} = \frac{G_F^2\alpha^2|V_{tb}V_{ts}^*|^2q^2\sqrt{\lambda}\beta_l}{3.2^9m_{in}^3\pi^5}\Bigg[\left(1+\frac{2m_\ell^2}{q^2}\right)H^{1,M_f^T}\overline{H}^{1,M_f^T} + \left(1-\frac{4m_\ell^2}{q^2}\right)H^{2,M_f^T}\overline{H}^{2,M_f^T}\Bigg]. \tag{25}$$

Similarly, differential decay rate for $\Lambda_b\to\Lambda\ell^+\ell^-$ decay is calculated as

$$\begin{aligned}\frac{d\Gamma\left(\Lambda_b\to\Lambda\ell^+\ell^-\right)}{dq^2} = \frac{G_F^2\alpha^2|V_{tb}V_{ts}^*|^2q^2\sqrt{\lambda}\beta_l}{3.2^{10}m_{\Lambda_b}^3\pi^5}\Bigg[&\frac{2m_\ell^2}{q^2}3\Big\{\left|H_t^2(+1/2,-1/2)\right|^2 + \left|H_t^2(-1/2,+1/2)\right|^2\Big\} + \left(1+\frac{2m_\ell^2}{q^2}\right)\Big\{\left|H_+^1(+1/2,+1/2)\right|^2 \\ &+ \left|H_-^1(-1/2,-1/2)\right|^2 + \left|H_0^1(+1/2,-1/2)\right|^2 + \left|H_0^1(-1/2,+1/2)\right|^2\Big\} \\ &+ \left(1-\frac{4m_\ell^2}{q^2}\right)\Big\{\left|H_+^2(+1/2,+1/2)\right|^2 + \left|H_-^2(-1/2,-1/2)\right|^2 \\ &+ \left|H_0^2(+1/2,-1/2)\right|^2 + \left|H_0^2(-1/2,+1/2)\right|^2\Big\}\Bigg].\end{aligned} \tag{26}$$

The decay rate in Eq. (26) can be separated into two parts. The first part corresponding to Λ_b and Λ having opposite spins is denoted as $d\Gamma\left(\Lambda_b\to\Lambda^0\ell^+\ell^-\right)/dq^2$, while the other part with Λ_b and Λ having same spins is labelled as $d\Gamma\left(\Lambda_b\to\Lambda^1\ell^+\ell^-\right)/dq^2$. The LFUV observables are constructed by taking the ratio of decay rates for $M_{in}\to M_f\mu^+\mu^-$ and $M_{in}\to M_fe^+e^-$,

$$R_{M_f}\left[q^2_{\rm min},q^2_{\rm max}\right] = \frac{\int_{q^2_{\rm min}}^{q^2_{\rm max}} dq^2 d\Gamma(M_{in}\to M_f\mu^+\mu^-)/dq^2}{\int_{q^2_{\rm min}}^{q^2_{\rm max}} dq^2 d\Gamma(M_{in}\to M_fe^+e^-)/dq^2}. \tag{27}$$

For the vector and axial-vector final states, polarized LFUV ratios are defined as

$$R_{M_f^{L,T}}\left[q^2_{\min}, q^2_{\max}\right] = \frac{\int_{q^2_{\min}}^{q^2_{\max}} dq^2 d\Gamma(M_{in} \to M_f^{L,T}\mu^+\mu^-)/dq^2}{\int_{q^2_{\min}}^{q^2_{\max}} dq^2 d\Gamma(M_{in} \to M_f^{L,T}e^+e^-)/dq^2}. \tag{28}$$

Similarly, for $\Lambda_b \to \Lambda\ell^+\ell^-$ decay

$$R_{\Lambda}\left[q^2_{\min}, q^2_{\max}\right] = \frac{\int_{q^2_{\min}}^{q^2_{\max}} dq^2 d\Gamma(\Lambda_b \to \Lambda\mu^+\mu^-)/dq^2}{\int_{q^2_{\min}}^{q^2_{\max}} dq^2 d\Gamma(\Lambda_b \to \Lambda e^+e^-)/dq^2}, \tag{29}$$

$$R_{\Lambda^{0,1}}\left[q^2_{\min}, q^2_{\max}\right] = \frac{\int_{q^2_{\min}}^{q^2_{\max}} dq^2 d\Gamma(\Lambda_b \to \Lambda^{0,1}\mu^+\mu^-)/dq^2}{\int_{q^2_{\min}}^{q^2_{\max}} dq^2 d\Gamma(\Lambda_b \to \Lambda^{0,1}e^+e^-)/dq^2}. \tag{30}$$

5. Predictions for LFUV ratios in the SM and the NP scenarios

5.1. NP scenarios

To give predictions and perform numerical analysis of the LFUV ratios, we first specify our choice of the NP scenarios, from two sets of recent global fit [42,53][3] to the $b \to s\ell^+\ell^-$ data,[4] which could be easily realized in the specific simple NP models.

[3] Maximum likelihood fit with Gaussian distribution (or minimum χ^2 fit) has been utilized in [42,53] by treating the theoretical and experimental covariance matrices equally. In [42], it is specified that asymmetric uncertainties have been symmetrized by taking the largest uncertainty, while in [53] the fit was performed with the help of MINUIT [88], flavio [89] and Wilson [90] using the default configuration of these packages.

[4] These two sets of fit both have taken into account the measurements of LFUV ratios $R_{K^{(*)}}$, and differential branching ratios, angular observables and polarization fractions for various $b \to s\mu^+\mu^-$ channels, including $B \to K^{(*)}\mu^+\mu^-$, $B_s \to \phi\mu^+\mu^-$, $B \to X_s\mu^+\mu^-$ and $B_s \to \mu^+\mu^-$, measured by different collaborations including LHCb, CMS, ATLAS, Belle, BaBar and CDF. In the more recent analysis [42], further updates on R_K [37], branching ratios $\mathcal{B}(B^{0,+} \to K^{0,+}\mu^+\mu^-)$ [33] and $\mathcal{B}(B_s \to \mu^+\mu^-)$ [91], and angular distribution of $B^+ \to K^{(*)+}\mu^+\mu^-$ [92,93] and $B \to K^*e^+e^-$ [94] were also included. For details, see [42,53] and the references therein. For the calculation of observables, $B \to K^{(*)}$ form factors in [20] (LCSR) and [95] (LCSR+lattice QCD) were respectively adopted in [42] and [53] (using flavio), and $B_s \to \phi$ form factors in [79] (LCSR+lattice QCD) were used in both [42] and [53]. Besides, the charm loop effects identified in [20] were also considered in [42,53].

Table 5
Best-fit values of the Wilson coefficients, and the 1σ ranges of different NP scenarios with assumptions, such as, purely LFUV NP in $b \to s\mu^+\mu^-$, additional arbitrary LFUV NP in $b \to se^+e^-$ along with LFUV NP in $b \to s\mu^+\mu^-$, and both LFU and LFUV NP.

Scenario		Best-fit value	1σ
S1	$C_{9\mu}^{\rm NP}$	-1.06	$[-1.20, -0.91]$
S2	$C_{9\mu}^{\rm NP} = -C_{10\mu}^{\rm NP}$	-0.44	$[-0.52, -0.37]$
S3	$C_{9\mu}^{\rm NP} = -C_{10\mu}^{\rm NP}$	-0.67	$[-0.82, -0.52]$
	$C_{9e}^{\rm NP} = -C_{10e}^{\rm NP}$	-0.28	$[-0.48, -0.08]$
S4	$C_{9\mu}^{\rm NP} = -C_{10\mu}^{\rm NP}$	-0.64	$[-0.78, -0.50]$
	$C_{9e}^{\rm NP}$	-0.65	$[-1.09, -0.21]$
S5	$C_{9\mu}^{\rm V} = -C_{10\mu}^{\rm V}$	-0.30	$[-0.39, -0.21]$
	$C_{9}^{\rm U}$	-0.92	$[-1.10, -0.72]$
S6	$C_{9\mu}^{\rm V}$	-1.12	$[-1.28, -0.95]$
	$C_{10'}^{\rm U}$	-0.31	$[-0.46, -0.15]$

1) Assuming LFUV NP in $b \to s\mu^+\mu^-$ only, two basic (1D) NP scenarios (S1) $C_{9\mu}^{\rm NP}$ and (S2) $C_{9\mu}^{\rm NP} = -C_{10\mu}^{\rm NP}$, continue to provide better fit to all data, including the latest experimental inputs [42,53]. Therefore, for the S1 and S2 scenarios, we consider the best-fit Wilson coefficients from table-1 of Ref. [42], and collect them in Table 5, for the sake of completeness. S1 and S2 can be realized in the simplest NP models involving the tree-level exchange of a leptoquark (LQ) or a Z' boson. While S1 is only possible with a Z', S2 can appear in both LQ and Z' models [45].
2) Motivated by removing the tensions between the separate fits to LFD and LFUV observables, we consider the NP scenarios extending S1 and S2, with additional arbitrary LFUV NP in $b \to se^+e^-$, which affects only LFUV observables, leading to improved pulls with respect to the SM. While several scenarios extending S1 and S2, with the addition of one nonzero NP WC in $b \to se^+e^-$ are reported in [53], we pick only those scenarios, which can be realized in the context of the LQ and Z' models, and have improved pulls with respect to the SM, compared to the ones obtained in S1 and S2. Therefore, we consider S3 and S4 from table-4 of Ref. [53], that can be generated in Z' model, whereas only S3 can be realized in the LQ models due to the fact that leptoquarks can only contribute to $C_{9\ell}^{\rm NP} = -C_{10\ell}^{\rm NP}$, $\ell = e, \mu$. S3 and S4 are listed in Table 5.
3) Next, we consider the NP hypothesis which allows LFU NP (equal contributions for all the lepton flavours), in addition to LFUV contributions to muons only. NP Wilson coefficients in this case can be represented as

$$C^{\rm NP}_{i^{(\prime)}e} = C^{\rm U}_{i^{(\prime)}}, \qquad C^{\rm NP}_{i^{(\prime)}\mu} = C^{\rm U}_{i^{(\prime)}} + C^{\rm V}_{i^{(\prime)}\mu}, \tag{31}$$

with $i = 9, 10$, for the $b \to s\mu^+\mu^-$ and $b \to se^+e^-$ transitions, respectively. The superscript "U" and "V" represents the LFU and LFUV contribution, respectively. Several NP scenarios with both LFU and LFUV NP contributions are presented in table-4 of Ref. [42]. For the sake of simplicity, we restrict to the NP scenarios, which only extend S1 and S2, yielding equal or improved pulls compared to the corresponding ones for the S1 and S2 scenarios, given in table-1 of [42], and can be fairly easily realized in specific NP models. It is important to mention that one should be very careful while comparing pulls found in different analyses, as they strongly depend on the choice of observables, treatment of the theoretical errors, and the fact that how the analysis is performed. Therefore, we only consider comparison of pulls between scenarios obtained within a single analysis. Based on the above criteria, we consider S8 and S11 given in table-4 of [42], and label them as S5 and S6, as shown in Table 5. Scenario S5 can be generated via off-shell photon penguins [96] in a LQ model, while S6 can be generated in Z' model with vector couplings to muons and additional Vectorlike quarks with the quantum numbers of left-handed quarks doublets [97].

It is worth mentioning that the above two methods of considering additional $b \to se^+e^-$ NP are complementary and each NP scenario in one method can be translated into the other, and vice versa [98], however, they offer distinct fitting mechanism to LFD and LFUV observables and therefore may correspond to unique NP predictions. For example, it is suggested in Ref. [59], that assuming both LFU and LFUV NP provides a different mechanism to obey the constraint from the LFD observable $\mathcal{B}(B_s \to \mu^+\mu^-)$, with large value of $C^{\rm V}_{10\mu}$ WC with opposite sign $C^{\rm U}_{10}$ WC value, and hence allows the possibility of new class of NP models with large LFU and LFUV contributions to $C_{10\mu}$ at the same time, to account for the combined LFD+LFUV observables. This result is not obtained with only LFUV NP contributions to both $b \to s\mu^+\mu^-$ and $b \to se^+e^-$, as the additional LFUV NP in $b \to se^+e^-$, affects only LFUV observables and the LFD observables, in this case, explained only by the LFUV NP contributions to $b \to s\mu^+\mu^-$, lead to the other favoured NP scenarios with large pulls.

5.2. Predictions for the LFUV ratios

In this section, we explore the patterns of the lepton flavour universality violation, in different bins of the complementary ratios, due the presence of different NP possibilities in the form of the best-fit values of the Wilson coefficients, found in the recent global fit analyses. For that, we consider various LFUV ratios, including (pseudo-)scalar final states, R_{f_0}, $R_{K_0^*}$, R_K, unpolarized and polarized (axial-)vector final states, $R_{\phi^{(L,T)}}$, $R_{K^{*(L,T)}}$, $R_{K_1^{(L,T)}(1270,1400)}$, and Λ baryon final state with different spin orientations $R_{\Lambda^{(0,1)}}$. Experimentally, $R_{K^{(*)}}$ has already been measured by LHCb in the kinematical region $q^2 \leq 6$ GeV^2, and by Belle in the low and high q^2 regions with large errors. Future precision measurements of high q^2 bins at Belle II and LHCb will be complementary and important for testing LFU, therefore, in our analysis, we consider only high q^2 bins of $R_{K^{(*)}}$.

In Figs. 1-5, we show the SM and the NP predictions, for the LFUV ratios in the low q^2 bin, [0.045, 1] GeV^2, the central q^2 bin, [1, 6] GeV^2, and the high q^2 bin, [14, $q^2_{\rm max}$] GeV^2. The height of the bars in Figs. 1-5, represent the uncertainty in the SM and NP predictions due to the errors in the form factors. We explicitly list the central values predictions and the predictions

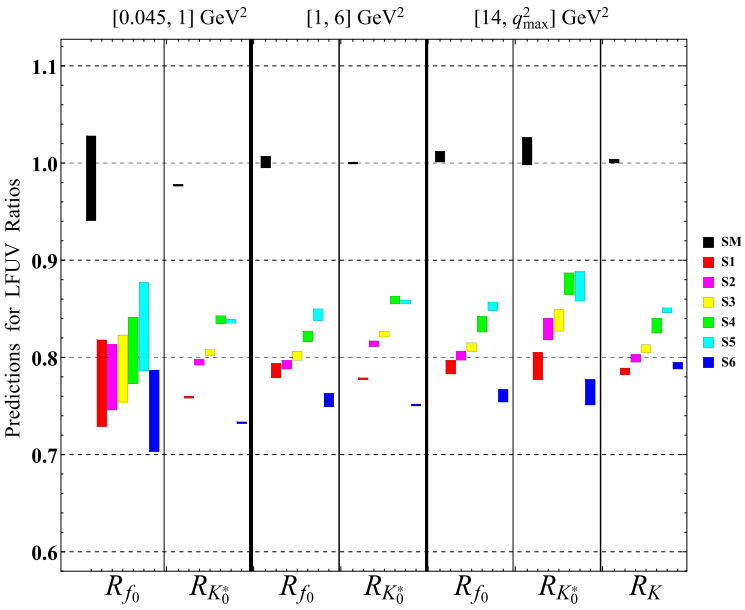

Fig. 1. Predictions for the LFUV ratios involving decays with scalar or pseudoscalar final state particles, R_{f_0}, $R_{K_0^*}$, and R_K. Three kinematical regions, low [0.045, 1] GeV^2, central [1, 6] GeV^2, and high [14, $q^2_{\rm max}$] GeV^2, are chosen, where $q^2_{\rm max} = 19.2$, 14.9, and 22.9 GeV^2, for R_{f_0}, $R_{K_0^*}$, and R_K, respectively. In each case, predictions from left to right, correspond to the SM and scenarios S1 to S6, depicted with different colours.

due to the errors in the form factors, for all the LFUV ratios in the SM and the NP scenarios, in Tables 7-13, of appendix F.

5.2.1. SM and NP predictions for R_S and R_P

In this section, we consider the LFUV ratios involving decays with scalar or pseudoscalar final states, R_{f_0}, $R_{K_0^*}$, and R_K. SM and NP predictions for these ratios are shown in Fig. 1. It is clear from Fig. 1, that in all q^2 bins, NP predictions for these ratios are considerably lower than the corresponding SM predictions. Considering, R_{f_0} first, the SM predictions of R_{f_0} in the central and high q^2 bins are relatively clean and these bins are also very useful to distinguish among the different NP scenarios except between S1 and S2 scenarios. This means that the NP sensitivities vary for the different scenarios with the highest NP sensitivity observed in scenario S6. Next, for $R_{K_0^*}$, SM values in the low and central q^2 bins are very clean therefore future measurements of $R_{K_0^*}$ in these bins have the potential to reveal NP unambiguously, however in order to differentiate the NP scenarios very precise measurements of $R_{K_0^*}$ will be required in these two bins as the form factor uncertainties in the presence of the NP scenarios also largely cancel out. On the other hand, the SM predictions in the low q^2 bin of R_{f_0}, and the high q^2 bin of $R_{K_0^*}$ are not clean and also the NP predictions involve large uncertainties, resulting in the frequent overlap of the different NP scenarios, making such bins less useful. In any case, NP predictions for R_{f_0} and $R_{K_0^*}$ should differ from the SM predictions, therefore it would be very useful for testing LFU by measuring them. In addition, very interestingly, the measurement of R_K at high q^2, which can be accessible at Belle II [99], can help to distinguish almost all NP scenarios, making such measurement very anticipated.

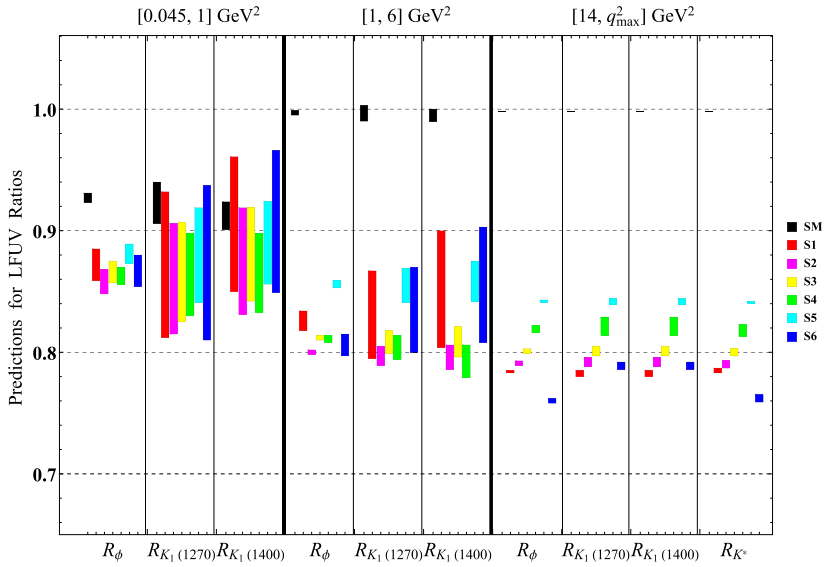

Fig. 2. Predictions for the LFUV ratios involving decays with vector or axial-vector final state particles, R_ϕ, R_{K^*}, $R_{K_1(1270)}$, and $R_{K_1(1400)}$, where only $R_{K_1(1270)}$ values with $\theta_{K_1} = -34^\circ$, and $R_{K_1(1400)}$ values with $\theta_{K_1} = 34^\circ$ are presented. Three kinematical regions, low $[0.045, 1]$ GeV^2, central $[1, 6]$ GeV^2, and high $[14, q^2_{\rm max}]$ GeV^2, are chosen, where $q^2_{\rm max} = 18.9$, 19.2, 16, and 15 GeV^2, for R_ϕ, R_{K^*}, $R_{K_1(1270)}$, and $R_{K_1(1400)}$ respectively. In each case, predictions from left to right, correspond to the SM and scenarios S1 to S6, depicted with different colours.

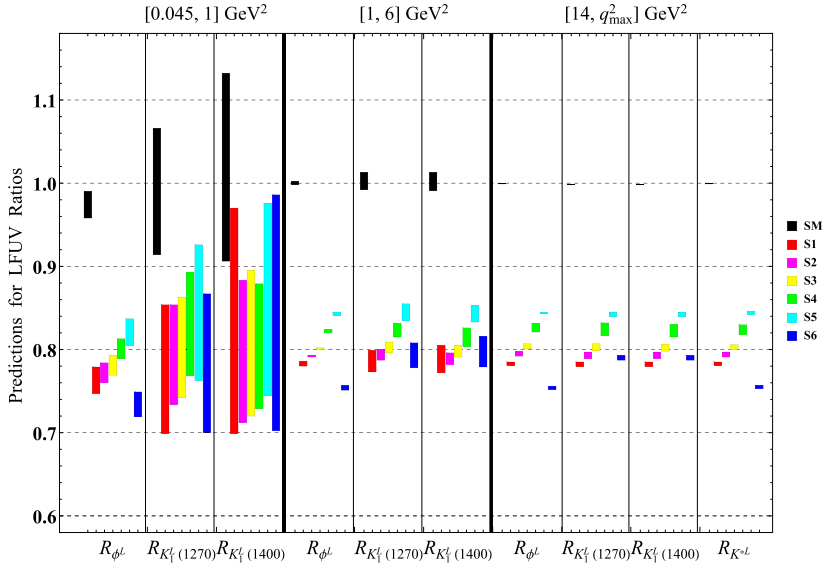

Fig. 3. Same as Fig. 2, where final state particles are longitudinally polarized, giving polarized LFUV ratios, R_{ϕ^L}, $R_{K^{*L}}$, $R_{K_1^L(1270)}$, and $R_{K_1^L(1400)}$.

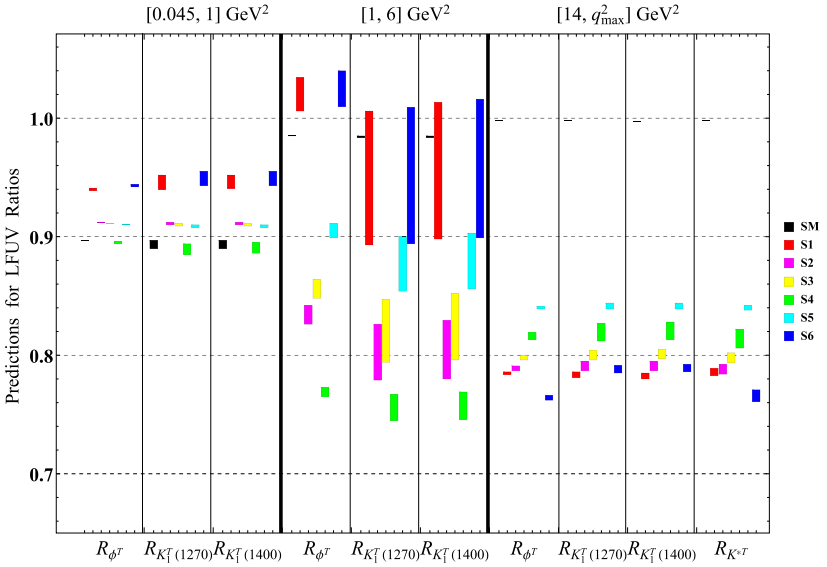

Fig. 4. Same as Fig. 2, where final state particles are transversely polarized, giving polarized LFUV ratios, R_{ϕ^T}, $R_{K^{*T}}$, $R_{K_1^T(1270)}$, and $R_{K_1^T(1400)}$.

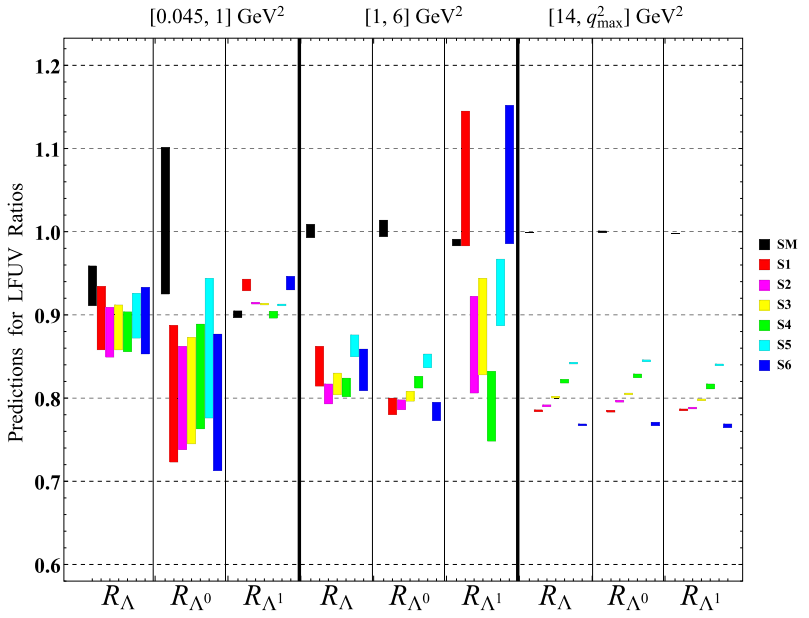

Fig. 5. Predictions for the LFUV ratios, R_Λ, R_{Λ^0}, and R_{Λ^1}, involving baryonic final state. Three kinematical regions, low [0.045, 1] GeV^2, central [1, 6] GeV^2, and high [14, $q^2_{\rm max}$] GeV^2, are chosen, where $q^2_{\rm max} = 20.3$ GeV^2. In each case, predictions from left to right, correspond to the SM and scenarios S1 to S6, depicted with different colours.

5.2.2. SM and NP predictions for $R_{V^{(L,T)}}$ and $R_{A^{(L,T)}}$

In this section, we consider the LFUV ratios involving decays with unpolarized and polarized vector or axial-vector final states, $R_{\phi^{(L,T)}}$, $R_{K^{*(L,T)}}$, $R_{K_1^{(L,T)}(1270)}$, and $R_{K_1^{(L,T)}(1400)}$. Before presenting our predictions, we need to specify what value of the K_1 mixing angle θ_{K_1}, we adopt. In fact, there are two widely used values, i.e., $\theta_{K_1} \sim -34^\circ$ [100], from $B \to K_1\gamma$ and $\tau \to K_1(1270)\nu$, and $\theta_{K_1} \sim 34^\circ$ [101,102], from the study of the $f_1(1285) - f_1(1420)$ and $h_1(1170) - h_1(1380)$ mixing.[5] These different possibilities of θ_{K_1} lead to different predictions for the observables. In the case of $\theta_{K_1} = -34^\circ$, the branching ratio of $\mathcal{B}(B \to K_1(1400)\ell^+\ell^-)$ is suppressed by one to two orders of magnitude with respect to $\mathcal{B}(B \to K_1(1270)\ell^+\ell^-)$, while in the case of $\theta_{K_1} = 34^\circ$, the situation is reversed, such that $\mathcal{B}(B \to K_1(1270)\ell^+\ell^-)$ is more suppressed. Given the highly suppressed decay modes are difficult to measure experimentally, we only present the enhanced mode for each possibility of θ_{K_1}, i.e., $B \to K_1(1270)\ell^+\ell^-$, for $\theta = -34^\circ$, and $B \to K_1(1400)\ell^+\ell^-$, for $\theta = 34^\circ$. In fact, these two cases have very analogous predictions for R_{K_1} as can be seen in the subsequent analysis.

In Fig. 2, we present the SM and the NP predictions for the unpolarized LFUV ratios, R_ϕ, R_{K^*}, and $R_{K_1(1270,\,1400)}$. SM predictions of these LFUV ratios in the central and high q^2 region are close to one, while in the low q^2 region [0.045, 1] GeV^2, due to non-negligible lepton mass effects [31], they are less than one. Further, considering the SM predictions, in the low q^2 bin [0.045, 1] GeV^2, it is important to mention that the involved branching fractions in these LFUV ratios are dominated by $C_{7^{(\prime)}}$, instead of $C_{9,10}$, and these magnetic dipole Wilson coefficients enter in the helicity amplitudes corresponding to the vector leptonic current. However, compared to C_7, $C_{7'}$ is still m_s/m_b suppressed, and therefore we have ignored it for the SM predictions of these unpolarized LFUV ratios. Furthermore, for the NP predictions, in the low q^2 region, although the branching fractions are highly sensitive to NP scenarios $C_{7^{(\prime)}}^{\rm NP}$, contributions of these radiative coefficients $C_{7^{(\prime)}}^{\rm NP}$ to the LFUV ratios, involving both muons and electrons, are lepton flavor universal, and therefore they can only play a subleading role in interference terms involving additional semileptonic NP coefficients [49]. So, in our study, we do not further consider scenarios with $C_{7^{(\prime)}}^{\rm NP}$, and for the NP predictions of these unpolarized LFUV ratios, in the low q^2 region, we use the already selected NP scenarios.

In Fig. 2, we observe that in the low q^2 region [0.045, 1] GeV^2, R_ϕ is able to discriminate between the SM and the NP values although it cannot distinguish any specific NP scenario, and on the contrary $R_{K_1(1270,\,1400)}$, in the same q^2 bin, do not have good sensitivity to NP as the NP predictions overlap with the SM ranges, which also have relatively large uncertainties. With the increase of the momentum transfer, R_ϕ and R_{K_1} become more sensitive to NP, and in the central q^2 region [1, 6] GeV^2, R_ϕ can distinguish S1 and S5, while $R_{K_1(1270,\,1400)}$ are not able to discriminate any specific NP scenario. The measurement of R_ϕ in this region is very useful given the statistical uncertainty can be less than 0.05 after 50 fb^{-1} data is accumulated at LHCb [104]. Furthermore, in the high q^2 region, sensitivity to NP becomes even more clear as both R_ϕ and $R_{K_1(1270,\,1400)}$ have very small errors for the SM and NP predictions, and thus should be able to distinguish among most NP scenarios except between S2 and S6 in case of $R_{K_1(1270,\,1400)}$. Besides, the high q^2 bin of R_{K^*} is also very useful for differentiating among the NP scenarios, therefore future measurements of both R_K and R_{K^*} in high q^2 region would be crucial for probing NP signature in the form of LFUV, given the Belle II sensitivities are less than 4% with 50 ab^{-1} data [99].

[5] It has been proposed in [103] to extract the K_1 mixing angle from $\tau^- \to K_1^-\nu_\tau \to (K^-\omega)\nu_\tau \to (K^-\pi^+\pi^-\pi^0)\nu_\tau$.

Additionally, in Fig. 3, we show the results for the LFUV ratios in the presence of NP scenarios, with the final vector and axial-vector states longitudinally polarized, R_{ϕ^L}, $R_{K_1^L(1270,1400)}$ and $R_{K^{*L}}$. These ratios can provide complementary information for testing the LFU. Although the ratios corresponding to longitudinally polarized final states, i.e., R_{ϕ^L}, $R_{K_1^L(1270,1400)}$ and $R_{K^{*L}}$ have similar behaviours with respect to R_ϕ, $R_{K_1(1270,1400)}$ and R_{K^*}, R_{ϕ^L} and $R_{K_1^L}$ are more sensitive to NP in the central q^2 region, with R_{ϕ^L} giving very distinct NP predictions for almost all the NP scenarios. In contrast, the LFUV ratios for transversely polarized final state mesons, as shown in Fig. 4, have even more interesting behaviours in the low q^2 region: they are sensitive to effects from the NP scenarios except S4 because in these scenarios they are greater than the SM predictions and with small errors. In the central q^2 region, R_{ϕ^T} in different NP scenarios except S1 and S6 is quite distinct and clearly distinguishable from the clean SM prediction with NP scenarios showing sensitivity to both the positive and negative side of the SM, while in the same q^2 bin $R_{K_1^T(1270,1400)}$ in different NP scenarios have relatively large errors, making it hard to discriminate among the NP scenarios except S4. In the high q^2 region, analogous to R_{ϕ^L}, $R_{K_1^L(1270,1400)}$ and $R_{K^{*L}}$, the ratios for transverse polarization R_{ϕ^T}, $R_{K_1^T(1270,1400)}$ and $R_{K^{*T}}$ in both the SM and the NP scenarios have relatively small errors and they provide very good sensitivity to test the lepton flavor universality.

5.2.3. SM and NP predictions for $R_{\Lambda(0,1)}$

In this section, we consider the LFUV ratios $R_{\Lambda(0,1)}$. SM and NP predictions for the scenarios S1-S6, for the ratios R_Λ, R_{Λ^0}, and R_{Λ^1} are presented in Fig. 5. It is observed that the behaviour of R_Λ and R_{Λ^0} is analogous in the sense that the large-recoil bins having low sensitivity to NP cannot distinguish among the different NP scenarios, the central q^2 bins with increased sensitivity to NP scenarios can partially distinguish the NP scenarios, and the low-recoil bins with distinct and clean SM and NP predictions can well distinguish all the NP scenarios. In contrast, for R_{Λ^1}, most NP scenarios are non-distinguishable by using the central q^2 bins, partially distinguishable by using the high-recoil bins and almost fully distinguishable by using the low-recoil bins. Therefore, the most remarkable conclusion on $R_{\Lambda(0,1)}$ is that it would be most helpful to measure the high q^2 bins of $R_{\Lambda(0,1)}$ because these bins have very small uncertainties. Lastly, similar to R_{ϕ^T}, R_{Λ^1} corresponding to S1 and S6, in central q^2 region may exceed 1, which can be an interesting characteristic for these scenarios, although they are not distinguishable from each other.

6. Summary and conclusions

In recent years, a number of experimental measurements for the $b \to s\ell^+\ell^-$ transitions have shown deviations from the SM expectations. Such measurements include the branching ratios $\mathcal{B}(B \to K^{(*)}\mu^+\mu^-)$ and $\mathcal{B}(B_s \to \phi\mu^+\mu^-)$, the angular observables in $B \to K^*\mu^+\mu^-$ decay including the famous P_5' anomaly, and very importantly, the LFUV ratios $R_{K^{(*)}}$ which are "clean" probe for LFUV/NP. On the other hand, experimental measurements of the LFUV ratios for either more $b \to s\ell^+\ell^-$ channels or more kinematical regions at Belle II and LHCb have been put on the agenda [99,104]. In light of the current stage, we have studied the LFUV ratios for various $b \to s\ell^+\ell^-$ channels with (pseudo-)scalar and (axial-)vector final state mesons including R_{f_0}, $R_{K_0^*}$, R_K, R_{K^*}, R_ϕ, R_{K_1} as well as R_Λ for $\Lambda_b \to \Lambda\ell^+\ell^-$. In particular, for the cases when spin-1 meson or the Λ baryon is the final state, we have also considered the LFUV ratios with the final state hadron longitudinally and transversally polarized.

In our calculation, we have adopted the recent results of hadronic form factors calculated in lattice QCD or/and QCD light-cone sum rules (LCSR). Within the framework of the effective field theory, we have studied various decay channels by employing the helicity formalism, and give the expressions of the physical observables in terms of the helicity amplitudes by keeping lepton mass effects. Further, we have explicitly worked out the expressions of the helicity amplitudes in terms of the (NP) Wilson coefficients and the general hadronic form factors, in a consistent manner, by using the same kinematical configuration and polarization conventions for all the decay channels, which allows others to easily check and use our expressions.

In the numerical analysis, we have made predictions and performed analysis for the SM and the selected NP scenarios. Given the updated measurements of $R_{K^{(*)}}$ suggest NP also present in $b \to se^+e^-$, therefore, besides considering the two basic $b \to s\mu^+\mu^-$ NP scenarios S1 ($C_{9\mu}^{\rm NP}$ only) or S2 ($C_{9\mu}^{\rm NP} = -C_{10\mu}^{\rm NP}$), we have also considered four NP scenarios which extend S1 and S2, assuming additional arbitrary LFUV NP in $b \to se^+e^-$ or both LFU and LFUV NP, and have explicit model interpretations. These scenarios are two $b \to s\mu^+\mu^-$ plus $b \to se^+e^-$ NP scenarios S3 and S4, and two LFU plus LFUV NP scenarios S5 and S6. The conclusions can be summarized as follows:

- $R_{K^{(*)}}$ in the high q^2 region have quite good sensitivity to NP, therefore future precision measurements on the high q^2 bins will be important complement to the measurements of low q^2 bins in probing LFUV/NP in the $b \to s\ell^+\ell^-$ transition.
- Measurements of the LFUV ratios with scalar mesons in final states are also very helpful for distinguishing NP scenarios. In particular, R_{f_0} in the bins [1, 6] GeV^2 and [14, $q^2_{\rm max}$] GeV^2, and $R_{K_0^*}$ in the bins [0.045, 1] GeV^2 and [1, 6] GeV^2 are useful because the theoretical uncertainties in these bins are relatively small compared with other bins.
- R_ϕ is useful for testing LFUV/NP in all kinematical regions and especially in the high q^2 region where theoretical predictions have small errors and the different NP scenarios have distinct predictions. In contrast, R_{K_1} in the SM and NP scenarios have larger errors in the low and central q^2 bins and it has good sensitivity to NP in the central and high q^2 region, with NP scenarios more distinct in the high q^2 region.
- R_{ϕ^L} and $R_{K_1^L}$ corresponding to longitudinally polarized final state meson have similar behaviours with respect to the unpolarized ratios R_ϕ and R_{K_1} in all q^2 bins, but for R_{ϕ^T} and $R_{K_1^T}$ corresponding to transversely polarized ϕ and K_1, the low and high q^2 bins have less uncertainties in the NP predictions, while the central q^2 bins NP predictions have large uncertainties.
- R_Λ, R_{Λ^0} and R_{Λ^1} are all very sensitive to NP with tiny theoretical errors in high q^2 region, which can test LFUV with distinct NP predictions. $R_{\Lambda^{(0,1)}}$, in the region [0.045, 1] GeV^2 do not have good sensitivity to NP, while in [1, 6] GeV^2, the measurements of R_{Λ^0} can distinguish some of the NP scenarios, e.g., the central q^2 bin of R_{Λ^0} can distinguish S4 and S5.

In conclusion, similar to $R_{K^{(*)}}$, SM predictions for the various complementary LFUV ratios are theoretically clean in different kinematical regions and have high sensitivity to NP. Therefore, the future measurements on the LFUV ratios for these additional channels, along with the more precise $R_{K^{(*)}}$ measurements, can provide critical information on testing NP/LFUV in the $b \to s\ell^+\ell^-$ FCNC transitions. In addition, LFUV ratios with polarized final state particles are also found to be sensitive to different NP scenarios, and therefore can provide additional

complementary probe of LFUV. With the running of Belle II and future upgrade of LHCb, the measurements of many LFUV ratios studied in this work will be accessible, especially $R_{K^{(*)}}$ in high q^2 region and R_ϕ which have already been planned [99,104]. We hope upcoming experimental and theoretical studies on the LFUV ratios in the $b \to s\ell^+\ell^-$ transitions, along with giving crucial evidence of possible NP behind the $b \to s\ell^+\ell^-$ anomalies, will also help to identify the true structure of the underlying NP, by differentiating among the emerging NP scenarios.

CRediT authorship contribution statement

The authors contributed equally to this work.

Declaration of competing interest

The authors declare that they have no known competing financial interests or personal relationships that could have appeared to influence the work reported in this paper.

Acknowledgements

F.M.B. would like to acknowledge the financial support from the Provincial Postdoctoral Talent Introduction Fund under Grant No. 2019YJ-01. The work is partly supported by National Science Foundation of China under the Grants 11775012, 11521505 and 11621131001. Z.R.H. would like to acknowledge the YST Program at the APCTP. M.A.P. would like to thank the hospitality provided by IHEP when this project was initiated. We would like to thank Yixiong Zhou for useful discussions.

Appendix A. SM Wilson coefficients

For the explicit form of the Wilson coefficients $C_7^{\rm eff}(q^2)$ and $C_9^{\rm eff}(q^2)$, we follow [69–74]. For the sake of completeness we give the expressions of these Wilson coefficients used in our study

$$\begin{aligned}
C_7^{\rm eff}(q^2) &= C_7 - \frac{1}{3}\left(C_3 + \frac{4}{3}C_4 + 20C_5 + \frac{80}{3}C_6\right) \\
&\quad - \frac{\alpha_s}{4\pi}\left[(C_1 - 6C_2)F_{1,c}^{(7)}(q^2) + C_8 F_8^{(7)}(q^2)\right], \\
C_9^{\rm eff}(q^2) &= C_9 + \frac{4}{3}\left(C_3 + \frac{16}{3}C_5 + \frac{16}{9}C_6\right) - h(0,q^2)\left(\frac{1}{2}C_3 + \frac{2}{3}C_4 + 8C_5 + \frac{32}{3}C_6\right) \\
&\quad - h(m_b^{\rm pole}, q^2)\left(\frac{7}{2}C_3 + \frac{2}{3}C_4 + 38C_5 + \frac{32}{3}C_6\right) \\
&\quad + h(m_c^{\rm pole}, q^2)\left(\frac{4}{3}C_1 + C_2 + 6C_3 + 60C_5\right) \\
&\quad - \frac{\alpha_s}{4\pi}\left[C_1 F_{1,c}^{(9)}(q^2) + C_2 F_{2,c}^{(9)}(q^2) + C_8 F_8^{(9)}(q^2)\right],
\end{aligned} \tag{A.1}$$

where the functions $h(m_q^{\rm pole}, q^2)$ with $q = c, b$, and functions $F_8^{(7,9)}(q^2)$ are defined in [70], while the functions $F_{1,c}^{(7,9)}(q^2)$, $F_{2,c}^{(7,9)}(q^2)$ are given in [72] for low q^2 and in [73] for high q^2. The quark masses appearing in all of these functions are defined in the pole scheme.

Appendix B. Hadronic matrix elements

The matrix elements for the process $M_{in} \to S\ell^+\ell^-$, where the parent particle $M_{in} = B_s$ or B, and the daughter particle S is a scalar meson 0^+, such as $S = f_0(980)$ or $K_0^*(1430)$, are given by

$$\langle f_0\big(K_0^*\big)(k)|\bar{s}\gamma_\mu\gamma_5 b|B_s\big(B\big)(p)\rangle = -i\Big[f_+^{f_0(K_0^*)}(q^2)P_\mu + f_-^{f_0(K_0^*)}(q^2)q_\mu\Big], \tag{B.1}$$

$$\begin{aligned}\langle f_0\big(K_0^*\big)(k)|\bar{s}i\sigma_{\mu\nu}q^\nu\gamma_5 b|B_s\big(B\big)(p)\rangle = &-i\frac{f_T^{f_0(K_0^*)}(q^2)}{\big(m_{B_s(B)} + m_{f_0(K_0^*)}\big)}\\ &\times\Big[q^2P_\mu - \Big(m^2_{B_s(B)} - m^2_{f_0(K_0^*)}\Big)q_\mu\Big],\end{aligned} \tag{B.2}$$

where $P_\mu = p_\mu + k_\mu$, and $q_\mu = p_\mu - k_\mu$. For the $B_s \to f_0(980)\ell^+\ell^-$ decay, $f_+^{f_0}$, $f_0^{f_0}$, $f_T^{f_0}$ form factors are used in the numerical analysis. For that $f_-^{f_0}(q^2)$ form factor can be expressed as

$$f_-^{f_0}(q^2) = \frac{m^2_{B_s} - m^2_{f_0}}{q^2}(f_0^{f_0}(q^2) - f_+^{f_0}(q^2)). \tag{B.3}$$

The matrix elements for the process $M_{in} \to P\ell^+\ell^-$, where both initial $M_{in} = B$, and final state meson $P = K$, are pseudoscalar in nature, can be expressed as

$$\langle K(k)|\bar{s}\gamma_\mu b|B(p)\rangle = f_+^K(q^2)P_\mu + f_-^K(q^2)q_\mu, \tag{B.4}$$

$$\langle K(k)|\bar{s}\sigma_{\mu\nu}q^\nu b|B(p)\rangle = -\frac{f_T^K(q^2)}{m_B + m_K}\Big[q^2P_\mu - \Big(m_B^2 - m_K^2\Big)q_\mu\Big]. \tag{B.5}$$

For the $B \to K\ell^+\ell^-$ decay, f_+^K, f_0^K, f_T^K form factors are used in the numerical analysis. Therefore, $f_-^K(q^2)$ form factor is decomposed using a similar expression to Eq. (B.3).

For the process $M_{in} \to V\ell^+\ell^-$, where the parent particle $M_{in} = B$ or B_s, and the daughter particle V is a vector meson 1^-, such as $V = K^*$ or ϕ, the matrix elements for such decays can be parameterized in terms of the form factors as

$$\Big\langle K^*\big(\phi\big)(k,\overline{\epsilon})\,\Big|\bar{s}\gamma_\mu b\Big|\,B\big(B_s\big)(p)\Big\rangle = \frac{2\epsilon_{\mu\nu\alpha\beta}}{m_{B(B_s)} + m_{K^*(\phi)}}\overline{\epsilon}^{*\nu}p^\alpha k^\beta V^{K^*(\phi)}(q^2), \tag{B.6}$$

$$\begin{aligned}\Big\langle K^*\big(\phi\big)(k,\overline{\epsilon})\,\Big|\bar{s}\gamma_\mu\gamma_5 b\Big|\,B(B_s)(p)\Big\rangle = &\; i\left(m_{B(B_s)} + m_{K^*(\phi)}\right)g_{\mu\nu}\overline{\epsilon}^{*\nu}A_1^{K^*(\phi)}(q^2)\\ &- i\,P_\mu(\overline{\epsilon}^*\cdot q)\frac{A_2^{K^*(\phi)}(q^2)}{\big(m_{B(B_s)} + m_{K^*(\phi)}\big)}\\ &- i\,\frac{2m_{K^*(\phi)}}{q^2}q_\mu(\overline{\epsilon}^*\cdot q)\Big[A_3^{K^*(\phi)}(q^2) - A_0^{K^*(\phi)}(q^2)\Big],\end{aligned} \tag{B.7}$$

where

$$A_3^{K^*(\phi)}(q^2) = \frac{m_{B(B_s)} + m_{K^*(\phi)}}{2m_{K^*(\phi)}}A_1^{K^*(\phi)}(q^2) - \frac{m_{B(B_s)} - m_{K^*(\phi)}}{2m_{K^*(\phi)}}A_2^{K^*(\phi)}(q^2), \tag{B.8}$$

with $A_3(0) = A_0(0)$. Here and throughout the whole study, we have used $\epsilon_{0123} = +1$ convention for the Levi-Civita tensor. The additional form factors are the tensor form factors which can be expressed as

$$\left\langle K^*(\phi)(k,\overline{\epsilon})\left|\bar{s}i\sigma_{\mu\nu}q^\nu b\right|B(B_s)(p)\right\rangle = -2\epsilon_{\mu\nu\alpha\beta}\overline{\epsilon}^{*\nu}p^\alpha k^\beta T_1^{K^*(\phi)}(q^2), \tag{B.9}$$

$$\begin{aligned}\left\langle K^*(\phi)(k,\overline{\epsilon})\left|\bar{s}i\sigma_{\mu\nu}q^\nu\gamma_5 b\right|B(B_s)(p)\right\rangle &= i\Big[\left(m^2_{B(B_s)}-m^2_{K^*(\phi)}\right)g_{\mu\nu}\overline{\epsilon}^{*\nu}\\ &\quad-(\overline{\epsilon}^*\cdot q)P_\mu\Big]T_2^{K^*(\phi)}(q^2)+i(\overline{\epsilon}^*\cdot q)\\ &\quad\times\left[q_\mu-\frac{q^2}{m^2_{B(B_s)}-m^2_{K^*(\phi)}}P_\mu\right]T_3^{K^*(\phi)}(q^2).\end{aligned} \tag{B.10}$$

The relations between the form factors in [79], and the form factors given in above matrix elements are

$$\begin{aligned}A_{12}^{K^*(\phi)} &= \frac{\left(m_{B(B_s)}+m_{K^*(\phi)}\right)^2\left(m^2_{B(B_s)}-m^2_{K^*(\phi)}-q^2\right)A_1^{K^*(\phi)}-\lambda A_2^{K^*(\phi)}}{16m_{B(B_s)}m^2_{K^*(\phi)}\left(m_{B(B_s)}+m_{K^*(\phi)}\right)},\\ T_{23}^{K^*(\phi)} &= \frac{\left(m^2_{B(B_s)}-m^2_{K^*(\phi)}\right)\left(m^2_{B(B_s)}+3m^2_{K^*(\phi)}-q^2\right)T_2^{K^*(\phi)}-\lambda T_3^{K^*(\phi)}}{8m_{B(B_s)}m^2_{K^*(\phi)}\left(m_{B(B_s)}-m_{K^*(\phi)}\right)}.\end{aligned} \tag{B.11}$$

For $M_{in}\to A\ell^+\ell^-$ decay, where $M_{in}=B$, and $M_f=A$, is a final state axial vector meson 1^+, such as $K_1(1270,1400)$ meson. For this decay the matrix element can be parameterized in terms of transition form factors as follows

$$\begin{aligned}\langle K_1(k,\overline{\epsilon})|\bar{s}\gamma_\mu b|B(p)\rangle &= -\left(m_B+m_{K_1}\right)g_{\mu\nu}\overline{\epsilon}^{*\nu}V_1^{K_1}(q^2)+P_\mu(\overline{\epsilon}^*\cdot q)\frac{V_2^{K_1}(q^2)}{\left(m_B+m_{K_1}\right)}\\ &\quad+\frac{2m_{K_1}}{q^2}q_\mu(\overline{\epsilon}^*\cdot q)[V_3^{K_1}(q^2)-V_0^{K_1}(q^2)],\end{aligned} \tag{B.12}$$

$$\langle K_1(k,\overline{\epsilon})|\bar{s}\gamma_\mu\gamma_5 b|B(p)\rangle = \frac{2i\epsilon_{\mu\nu\alpha\beta}}{m_B+m_{K_1}}\overline{\epsilon}^{*\nu}p^\alpha k^\beta A^{K_1}(q^2), \tag{B.13}$$

where

$$\begin{aligned}V_3^{K_1}(q^2) &= \frac{m_B+m_{K_1}}{2m_{K_1}}V_1^{K_1}(q^2)-\frac{m_B-m_{K_1}}{2m_{K_1}}V_2^{K_1}(q^2),\\ V_3^{K_1}(0) &= V_0^{K_1}(0).\end{aligned} \tag{B.14}$$

The other contributions from the tensor form factors are

$$\begin{aligned}\langle K_1(k,\overline{\epsilon})|\bar{s}i\sigma_{\mu\nu}q^\nu b|B(p)\rangle &= \left[\left(m_B^2-m_{K_1}^2\right)g_{\mu\nu}\overline{\epsilon}^{*\nu}-(\overline{\epsilon}^*\cdot q)P_\mu\right]T_2^{K_1}(q^2)\\ &\quad+(\overline{\epsilon}^*\cdot q)\left[q_\mu-\frac{q^2}{m_B^2-m_{K_1}^2}P_\mu\right]T_3^{K_1}(q^2),\end{aligned} \tag{B.15}$$

$$\langle K_1(k,\overline{\epsilon})|\bar{s}i\sigma_{\mu\nu}q^\nu\gamma_5 b|B(p)\rangle = 2i\epsilon_{\mu\nu\alpha\beta}\overline{\epsilon}^{*\nu}p^\alpha k^\beta T_1^{K_1}(q^2)\,. \tag{B.16}$$

The matrix elements for the process $\Lambda_b\to\Lambda\ell^+\ell^-$, where both initial $M_{in}=\Lambda_b$, and final state baryon Λ, are spin half particles, can be conveniently written in the helicity basis

$$\left\langle\Lambda(k,s_\Lambda)\left|\bar{s}\gamma_\mu b\right|\Lambda_b(p,s_{\Lambda_b})\right\rangle = \bar{u}_\Lambda(k,s_\Lambda)\Big[f_t^V(q^2)(m_{\Lambda_b}-m_\Lambda)\frac{q_\mu}{q^2}$$

$$+ f_0^V(q^2)\frac{m_{\Lambda_b}+m_\Lambda}{s_+}\Big\{p_\mu + k_\mu - \frac{q_\mu}{q^2}(m^2_{\Lambda_b}-m^2_\Lambda)\Big\}$$
$$+ f_\perp^V(q^2)\Big\{\gamma_\mu - \frac{2m_\Lambda}{s_+}p_\mu - \frac{2m_{\Lambda_b}}{s_+}k_\mu\Big\}\Big]u_{\Lambda_b}(p,s_{\Lambda_b}), \tag{B.17}$$

$$\big\langle\Lambda(k,s_\Lambda)\,\big|\bar{s}\gamma_\mu\gamma_5 b\big|\,\Lambda_b(p,s_{\Lambda_b})\big\rangle = -\bar{u}_\Lambda(k,s_\Lambda)\gamma_5\Big[f_t^A(q^2)(m_{\Lambda_b}+m_\Lambda)\frac{q_\mu}{q^2}$$
$$+ f_0^A(q^2)\frac{m_{\Lambda_b}-m_\Lambda}{s_-}\Big\{p_\mu + k_\mu - \frac{q_\mu}{q^2}(m^2_{\Lambda_b}-m^2_\Lambda)\Big\}$$
$$+ f_\perp^A(q^2)\Big\{\gamma_\mu + \frac{2m_\Lambda}{s_-}p_\mu - \frac{2m_{\Lambda_b}}{s_-}k_\mu\Big\}\Big]u_{\Lambda_b}(p,s_{\Lambda_b}), \tag{B.18}$$

where we have $s\pm = (m_{\Lambda_b} \pm m_\Lambda)^2 - q^2$. Additionally,

$$\langle\Lambda(k,s_\Lambda)|\bar{s}i\sigma_{\mu\nu}\gamma^\nu b|\Lambda_b(p,s_{\Lambda_b})\rangle$$
$$= -\bar{u}_\Lambda(k,s_\Lambda)\Big[f_0^T(q^2)\frac{q^2}{s_+}\Big\{p_\mu + k_\mu - \frac{q_\mu}{q^2}(m^2_{\Lambda_b}-m^2_\Lambda)\Big\}$$
$$+ f_\perp^T(q^2)(m_{\Lambda_b}+m_\Lambda)\Big\{\gamma_\mu - \frac{2m_\Lambda}{s_+}p_\mu - \frac{2m_{\Lambda_b}}{s_+}k_\mu\Big\}\Big]u_{\Lambda_b}(p,s_{\Lambda_b}), \tag{B.19}$$

$$\langle\Lambda(k,s_\Lambda)|\bar{s}i\sigma_{\mu\nu}\gamma^\nu\gamma_5 b|\Lambda_b(p,s_{\Lambda_b})\rangle$$
$$= -\bar{u}_\Lambda(k,s_\Lambda)\gamma_5\Big[f_0^{T_5}(q^2)\frac{q^2}{s_-}\Big\{p_\mu + k_\mu - \frac{q_\mu}{q^2}(m^2_{\Lambda_b}-m^2_\Lambda)\Big\}$$
$$+ f_\perp^{T_5}(q^2)(m_{\Lambda_b}-m_\Lambda)\Big\{\gamma_\mu + \frac{2m_\Lambda}{s_-}p_\mu - \frac{2m_{\Lambda_b}}{s_-}k_\mu\Big\}\Big]u_{\Lambda_b}(p,s_{\Lambda_b}). \tag{B.20}$$

Appendix C. Details on the kinematics

C.1. Kinematics

The decay $M_{in} \to M_f \ell^+\ell^-$ can be conveniently regarded as a quasi-two-body decay with $M_{in} \to M_f j_{\rm eff}$ followed by $j_{\rm eff} \to \ell^+\ell^-$, where effective current $j_{\rm eff}$, represents the off-shell boson. The polarization vectors of $j_{\rm eff}$ satisfy the orthonormality and completeness relations as discussed in section 3. With $M_{in}(p) \to M_f(k)\left(j_{\rm eff}(q) \to \ell^+(p_1)\ell^-(p_2)\right)$, we define momenta in the rest frame of the parent particle M_{in} as

$$p^\mu = (m_{in},0,0,0), \qquad k^\mu = (E_f,0,0,-|\vec{k}|), \qquad q^\mu = (q^0,0,0,+|\vec{k}|), \tag{C.1}$$

where we choose daughter particle M_f to be moving along the negative z direction, and

$$q^0 = \frac{m_{in}^2 - m_f^2 + q^2}{2m_{in}}, \qquad E_f = \frac{m_{in}^2 + m_f^2 - q^2}{2m_{in}}, \qquad |\vec{k}| = \frac{\sqrt{\lambda(m_{in}^2, m_f^2, q^2)}}{2m_{in}}, \tag{C.2}$$

where $\lambda(m_{in}^2, m_f^2, q^2)$ is the Källén function

$$\lambda(a,b,c) = a^2 + b^2 + c^2 - 2(ab + ac + bc). \tag{C.3}$$

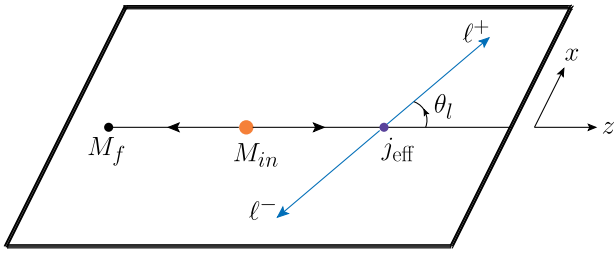

Fig. 6. Kinematics of the $M_{in} \to M_f \ell^+ \ell^-$ decay.

In the dilepton rest frame, considering $j_{\rm eff}$ decaying in the $x-z$ plane, and $\ell^+(p_1)$ lepton making angle θ_l with the z-axis (see Fig. 6),

$$\begin{aligned} p_1^\mu &= (E_l, |\vec{p}_l| \sin\theta_l, 0, |\vec{p}_l| \cos\theta_l), \\ p_2^\mu &= (E_l, -|\vec{p}_l| \sin\theta_l, 0, -|\vec{p}_l| \cos\theta_l), \end{aligned} \tag{C.4}$$

with

$$E_l = \frac{\sqrt{q^2}}{2}, \qquad |\vec{p}_l| = \frac{\sqrt{q^2}}{2}\beta_l, \qquad \beta_l = \sqrt{1 - \frac{4m_l^2}{q^2}}. \tag{C.5}$$

C.2. Polarization conventions

In the M_{in} rest frame, the polarization four-vectors of the effective current ($j_{\rm eff}$), that decays to dilepton pair are

$$\begin{aligned} &\varepsilon^\mu(t) = \frac{1}{\sqrt{q^2}}(q^0, 0, 0, |\vec{k}|), \quad \varepsilon^\mu(\pm) = \frac{1}{\sqrt{2}}(0, \mp 1, -i, 0), \\ &\varepsilon^\mu(0) = \frac{1}{\sqrt{q^2}}(|\vec{k}|, 0, 0, q^0), \end{aligned} \tag{C.6}$$

and in the dilepton pair rest frame the transverse polarizations of $j_{\rm eff}$ remain same, while the time like and longitudinal polarizations read

$$\varepsilon^\mu(t) = (1, 0, 0, 0), \qquad \varepsilon^\mu(0) = (0, 0, 0, 1). \tag{C.7}$$

Similarly, when the final state is vector or axial-vector particle, the polarization four-vectors of $V(A)$ state moving along the negative z direction, in the M_{in} rest frame are

$$\overline{\epsilon}^\mu(\pm) = \frac{1}{\sqrt{2}}(0, \pm 1, -i, 0), \quad \overline{\epsilon}^\mu(0) = \frac{1}{m_f}(|\vec{k}|, 0, 0, E_f). \tag{C.8}$$

Transverse polarizations of $V(A)$ in its own rest frame remain same, whereas the longitudinal polarization reads

$$\overline{\epsilon}^\mu(0) = (0, 0, 0, -1). \tag{C.9}$$

Appendix D. Numerical inputs

In Table 6 we give the numerical values of the input parameters used in our study.

Table 6
Default values of the used input parameters. Values of some parameters are strongly scale dependent, but most of these parameters cancel in the LFUV ratios.

$G_F = 1.1663787 \times 10^{-5}$ GeV^{-2}	[105]	$m_B = 5.279$ GeV	[105]
$\lvert V_{tb}V_{ts}^*\rvert = 0.0397^{+0.0008}_{-0.0006}$	[105]	$m_{B_s} = 5.367$ GeV	[105]
$m_b = 4.18^{+0.03}_{-0.02}$ GeV	[105]	$\tau_B = (1.519 \pm 0.004) \times 10^{-12}$ s	[105]
$\alpha(m_b) = 1/133.28$	[83]	$\tau_{B_s} = (1.515 \pm 0.004) \times 10^{-12}$ s	[105]
$\alpha_s(m_b) = 0.2233$	[83]	$m_{f_0} = 0.990$ GeV	[105]
$m_e = 0.0005$ GeV	[105]	$m_{K_0^*} = 1.425$ GeV	[105]
$m_\mu = 0.106$ GeV	[105]	$m_K = 0.498$ GeV	[105]
$m_b^{\text{pole}} = 4.91 \pm 0.12$ GeV	[106]	$m_{K^*} = 0.896$ GeV	[105]
$m_c^{\text{pole}} = 1.77 \pm 0.14$ GeV	[106]	$m_\phi = 1.020$ GeV	[105]
$\mu_b = 5$ GeV	[74]	$m_{K_{1A}} = 1.31$ GeV	[107]
$m_{\Lambda_b} = 5.619$ GeV	[105]	$m_{K_{1B}} = 1.34$ GeV	[107]
$m_\Lambda = 1.116$ GeV	[105]	$m_{K_1(1270)} = 1.272$ GeV	[102]
$\tau_{\Lambda_b} = (1.471 \pm 0.009) \times 10^{-12}$ s	[105]	$m_{K_1(1400)} = 1.403$ GeV	[105]

Appendix E. $\Lambda_b \to \Lambda$ spinor bilinears

To calculate the hadronic helicity amplitudes for $\Lambda_b \to \Lambda \ell^+ \ell^-$ decay, we use the spinor representations given in [108,109]. For scalar and pseudo-scalar currents, we get

$$\begin{aligned}
&\bar{u}_\Lambda(k, \pm 1/2) u_{\Lambda_b}(p, \pm 1/2) = 0,\\
&\bar{u}_\Lambda(k, \pm 1/2) u_{\Lambda_b}(p, \mp 1/2) = \pm\sqrt{s_+},\\
&\bar{u}_\Lambda(k, \pm 1/2) \gamma_5 u_{\Lambda_b}(p, \pm 1/2) = 0\\
&\bar{u}_\Lambda(k, \pm 1/2) \gamma_5 u_{\Lambda_b}(p, \pm 1/2) = -\sqrt{s_-},
\end{aligned} \tag{E.1}$$

and for vector and axial-vector currents, we obtain

$$\begin{aligned}
&\bar{u}_\Lambda(k, \pm 1/2) \gamma^\mu u_{\Lambda_b}(p, \pm 1/2) = \mp\sqrt{2s_-}\epsilon^\mu(\pm),\\
&\bar{u}_\Lambda(k, \pm 1/2) \gamma^\mu u_{\Lambda_b}(p, \mp 1/2) = \pm(\sqrt{s_+}, 0, 0, -\sqrt{s_-}),\\
&\bar{u}_\Lambda(k, \pm 1/2) \gamma^\mu \gamma_5 u_{\Lambda_b}(p, \pm 1/2) = -\sqrt{2s_+}\epsilon^\mu(\pm)\\
&\bar{u}_\Lambda(k, \pm 1/2) \gamma^\mu \gamma_5 u_{\Lambda_b}(p, \mp 1/2) = (\sqrt{s_-}, 0, 0, -\sqrt{s_+}).
\end{aligned} \tag{E.2}$$

Appendix F. Predicted values of the LFUV ratios

In this appendix, we give the predicted central values with errors for the various LFUV ratios.

Table 7
SM and NP predictions for the LFUV ratio R_{f_0} in different bins. The first errors listed are due to the uncertainties of the form factors, and the second errors are due to the 1σ range of the best-fit Wilson coefficients in different NP scenarios.

Observable	Scenario	$q^2/\text{GeV}^2 : [0.045, 1]$	$q^2/\text{GeV}^2 : [1, 6]$	$q^2/\text{GeV}^2 : [14, q^2_{\text{max}}]$
R_{f_0}	SM	$0.977^{+0.051}_{-0.036}$	$1.000^{+0.007}_{-0.005}$	$1.006^{+0.006}_{-0.005}$
R_{f_0}	S1	$0.766^{+0.052(+0.025)}_{-0.037(-0.023)}$	$0.785^{+0.009(+0.026)}_{-0.006(-0.024)}$	$0.789^{+0.008(+0.026)}_{-0.006(-0.024)}$
R_{f_0}	S2	$0.774^{+0.039(+0.022)}_{-0.028(-0.025)}$	$0.792^{+0.005(+0.022)}_{-0.004(-0.025)}$	$0.802^{+0.004(+0.022)}_{-0.005(-0.025)}$
R_{f_0}	S3	$0.783^{+0.040(+0.078)}_{-0.029(-0.078)}$	$0.801^{+0.005(+0.080)}_{-0.004(-0.080)}$	$0.811^{+0.004(+0.078)}_{-0.005(-0.078)}$
R_{f_0}	S4	$0.802^{+0.039(+0.093)}_{-0.029(-0.093)}$	$0.821^{+0.006(+0.096)}_{-0.005(-0.096)}$	$0.835^{+0.007(+0.097)}_{-0.009(-0.097)}$
R_{f_0}	S5	$0.824^{+0.053(+0.032)}_{-0.038(-0.032)}$	$0.843^{+0.007(+0.033)}_{-0.005(-0.033)}$	$0.852^{+0.005(+0.032)}_{-0.004(-0.032)}$
R_{f_0}	S6	$0.738^{+0.049(+0.032)}_{-0.035(-0.030)}$	$0.755^{+0.008(+0.032)}_{-0.006(-0.031)}$	$0.760^{+0.007(+0.033)}_{-0.006(-0.031)}$

Table 8
SM and NP predictions for the LFUV ratio $R_{K_0^*}$ in different bins. The first errors listed are due to the uncertainties of the form factors, and the second errors are due to the 1σ range of the best-fit Wilson coefficients in different NP scenarios.

Observable	Scenario	$q^2/\text{GeV}^2 : [0.045, 1]$	$q^2/\text{GeV}^2 : [1, 6]$	$q^2/\text{GeV}^2 : [14, q^2_{\text{max}}]$
$R_{K_0^*}$	SM	0.977 ± 0.001	1.000 ± 0.001	1.012 ± 0.014
$R_{K_0^*}$	S1	$0.759 \pm 0.001^{(+0.027)}_{(-0.025)}$	$0.778 \pm 0.001^{(+0.028)}_{(-0.026)}$	$0.791 \pm 0.014^{(+0.028)}_{(-0.026)}$
$R_{K_0^*}$	S2	$0.795 \pm 0.003^{(+0.019)}_{(-0.022)}$	$0.814 \pm 0.003^{(+0.020)}_{(-0.023)}$	$0.829 \pm 0.011^{(+0.020)}_{(-0.022)}$
$R_{K_0^*}$	S3	$0.805 \pm 0.003^{(+0.070)}_{(-0.070)}$	$0.824 \pm 0.003^{(+0.072)}_{(-0.072)}$	$0.838 \pm 0.011^{(+0.071)}_{(-0.071)}$
$R_{K_0^*}$	S4	$0.839 \pm 0.004^{(+0.098)}_{(-0.098)}$	$0.859 \pm 0.004^{(+0.100)}_{(-0.100)}$	$0.876 \pm 0.011^{(+0.101)}_{(-0.101)}$
$R_{K_0^*}$	S5	$0.837 \pm 0.002^{(+0.029)}_{(-0.029)}$	$0.857 \pm 0.002^{(+0.029)}_{(-0.029)}$	$0.873 \pm 0.015^{(+0.029)}_{(-0.029)}$
$R_{K_0^*}$	S6	$0.733 \pm 0.001^{(+0.033)}_{(-0.031)}$	$0.751 \pm 0.001^{(+0.034)}_{(-0.032)}$	$0.764 \pm 0.013^{(+0.034)}_{(-0.032)}$

Table 9
SM and NP predictions for the LFUV ratios R_K, $R_{K^{*(L,T)}}$ in the high q^2 bin. The first errors listed are due to the uncertainties of the form factors, and the second errors are due to the 1σ range of the best-fit Wilson coefficients in different NP scenarios.

Scenario	Observable	$q^2/\text{GeV}^2 : [14, q^2_{\text{max}}]$	Observable	$q^2/\text{GeV}^2 : [14, q^2_{\text{max}}]$
SM	R_K	$1.002^{+0.002}_{-0.002}$	R_{K*}	0.998 ± 0.000
S1	R_K	$0.785^{+0.004(+0.026)}_{-0.003(-0.024)}$	R_{K*}	$0.785 \pm 0.002^{(+0.025)}_{(-0.023)}$
S2	R_K	$0.800^{+0.003(+0.021)}_{-0.005(-0.024)}$	R_{K*}	$0.790 \pm 0.003^{(+0.022)}_{(-0.025)}$
S3	R_K	$0.810^{+0.003(+0.077)}_{-0.005(-0.077)}$	R_{K*}	$0.800 \pm 0.003^{(+0.080)}_{(-0.080)}$
S4	R_K	$0.834^{+0.006(+0.097)}_{-0.009(-0.097)}$	R_{K*}	$0.818 \pm 0.005^{(+0.094)}_{(-0.094)}$
S5	R_K	$0.849^{+0.002(+0.032)}_{-0.003(-0.032)}$	R_{K*}	$0.841 \pm 0.001^{(+0.033)}_{(-0.033)}$
S6	R_K	$0.791^{+0.004(+0.028)}_{-0.003(-0.026)}$	R_{K*}	$0.762 \pm 0.003^{(+0.030)}_{(-0.028)}$
SM	R_{K*L}	0.999 ± 0.000	R_{K*T}	0.998 ± 0.000
S1	R_{K*L}	$0.783 \pm 0.002^{(+0.026)}_{(-0.024)}$	R_{K*T}	$0.786 \pm 0.003^{(+0.025)}_{(-0.023)}$
S2	R_{K*L}	$0.794 \pm 0.003^{(+0.022)}_{(-0.025)}$	R_{K*T}	$0.788 \pm 0.004^{(+0.022)}_{(-0.025)}$
S3	R_{K*L}	$0.803 \pm 0.003^{(+0.079)}_{(-0.079)}$	R_{K*T}	$0.798 \pm 0.004^{(+0.080)}_{(-0.080)}$
S4	R_{K*L}	$0.824 \pm 0.006^{(+0.095)}_{(-0.095)}$	R_{K*T}	$0.814 \pm 0.008^{(+0.094)}_{(-0.094)}$
S5	R_{K*L}	$0.844 \pm 0.002^{(+0.032)}_{(-0.032)}$	R_{K*T}	$0.840 \pm 0.002^{(+0.033)}_{(-0.033)}$
S6	R_{K*L}	$0.755 \pm 0.002^{(+0.032)}_{(-0.030)}$	R_{K*T}	$0.766 \pm 0.005^{(+0.029)}_{(-0.028)}$

Table 10
SM and NP predictions for the LFUV ratios $R_{\phi(L,T)}$ in different bins. The first errors listed are due to the uncertainties of the form factors, and the second errors are due to the 1σ range of the best-fit Wilson coefficients in different NP scenarios.

Observable	Scenario	$q^2/\text{GeV}^2 : [0.045, 1]$	$q^2/\text{GeV}^2 : [1, 6]$	$q^2/\text{GeV}^2 : [14, q^2_{\text{max}}]$
R_ϕ	SM	0.927 ± 0.004	0.997 ± 0.002	0.998 ± 0.000
R_ϕ	S1	$0.872 \pm 0.013^{(+0.006)}_{(-0.005)}$	$0.826 \pm 0.008^{(+0.019)}_{(-0.018)}$	$0.784 \pm 0.001^{(+0.025)}_{(-0.024)}$
R_ϕ	S2	$0.858 \pm 0.010^{(+0.007)}_{(-0.008)}$	$0.800 \pm 0.002^{(+0.021)}_{(-0.024)}$	$0.791 \pm 0.002^{(+0.022)}_{(-0.025)}$
R_ϕ	S3	$0.866 \pm 0.009^{(+0.026)}_{(-0.026)}$	$0.812 \pm 0.002^{(+0.076)}_{(-0.076)}$	$0.801 \pm 0.002^{(+0.079)}_{(-0.079)}$
R_ϕ	S4	$0.863 \pm 0.007^{(+0.024)}_{(-0.024)}$	$0.811 \pm 0.003^{(+0.076)}_{(-0.076)}$	$0.819 \pm 0.003^{(+0.094)}_{(-0.094)}$
R_ϕ	S5	$0.881 \pm 0.008^{(+0.010)}_{(-0.010)}$	$0.856 \pm 0.003^{(+0.030)}_{(-0.030)}$	$0.842 \pm 0.001^{(+0.032)}_{(-0.032)}$
R_ϕ	S6	$0.867 \pm 0.013^{(+0.007)}_{(-0.006)}$	$0.806 \pm 0.009^{(+0.023)}_{(-0.022)}$	$0.760 \pm 0.002^{(+0.031)}_{(-0.029)}$
R_{ϕ^L}	SM	0.974 ± 0.016	1.000 ± 0.002	0.999 ± 0.000
R_{ϕ^L}	S1	$0.763 \pm 0.016^{(+0.025)}_{(-0.023)}$	$0.783 \pm 0.003^{(+0.026)}_{(-0.024)}$	$0.783 \pm 0.002^{(+0.026)}_{(-0.024)}$
R_{ϕ^L}	S2	$0.772 \pm 0.012^{(+0.021)}_{(-0.024)}$	$0.792 \pm 0.001^{(+0.022)}_{(-0.025)}$	$0.795 \pm 0.003^{(+0.022)}_{(-0.025)}$
R_{ϕ^L}	S3	$0.781 \pm 0.012^{(+0.078)}_{(-0.077)}$	$0.801 \pm 0.001^{(+0.079)}_{(-0.079)}$	$0.804 \pm 0.003^{(+0.078)}_{(-0.078)}$
R_{ϕ^L}	S4	$0.801 \pm 0.012^{(+0.094)}_{(-0.094)}$	$0.822 \pm 0.002^{(+0.096)}_{(-0.096)}$	$0.826 \pm 0.005^{(+0.096)}_{(-0.096)}$
R_{ϕ^L}	S5	$0.821 \pm 0.016^{(+0.032)}_{(-0.032)}$	$0.843 \pm 0.002^{(+0.033)}_{(-0.033)}$	$0.844 \pm 0.001^{(+0.032)}_{(-0.032)}$
R_{ϕ^L}	S6	$0.734 \pm 0.015^{(+0.032)}_{(-0.029)}$	$0.754 \pm 0.003^{(+0.033)}_{(-0.031)}$	$0.754 \pm 0.002^{(+0.032)}_{(-0.031)}$
R_{ϕ^T}	SM	0.897 ± 0.000	0.985 ± 0.000	0.998 ± 0.000
R_{ϕ^T}	S1	$0.940 \pm 0.001^{(+0.006)}_{(-0.006)}$	$1.020 \pm 0.014^{(+0.012)}_{(-0.011)}$	$0.785 \pm 0.001^{(+0.025)}_{(-0.023)}$
R_{ϕ^T}	S2	$0.912 \pm 0.000^{(+0.003)}_{(-0.003)}$	$0.834 \pm 0.008^{(+0.023)}_{(-0.026)}$	$0.789 \pm 0.002^{(+0.022)}_{(-0.025)}$
R_{ϕ^T}	S3	$0.911 \pm 0.000^{(+0.010)}_{(-0.010)}$	$0.856 \pm 0.008^{(+0.085)}_{(-0.085)}$	$0.798 \pm 0.002^{(+0.080)}_{(-0.080)}$
R_{ϕ^T}	S4	$0.895 \pm 0.001^{(+0.017)}_{(-0.017)}$	$0.769 \pm 0.004^{(+0.046)}_{(-0.046)}$	$0.816 \pm 0.003^{(+0.094)}_{(-0.094)}$
R_{ϕ^T}	S5	$0.910 \pm 0.000^{(+0.004)}_{(-0.004)}$	$0.905 \pm 0.006^{(+0.032)}_{(-0.032)}$	$0.840 \pm 0.001^{(+0.033)}_{(-0.033)}$
R_{ϕ^T}	S6	$0.943 \pm 0.001^{(+0.007)}_{(-0.007)}$	$1.025 \pm 0.015^{(+0.015)}_{(-0.014)}$	$0.764 \pm 0.002^{(+0.030)}_{(-0.028)}$

Table 11
SM and NP predictions for the LFUV ratios $R_{K_1^{(L,T)}(1270)}$, with $\theta_{K_1} = -34^\circ$, in different bins. The first errors listed are due to the uncertainties of the form factors, and the second errors are due to the 1σ range of the best-fit Wilson coefficients in different NP scenarios.

Observable	Scenario	$q^2/\text{GeV}^2 : [0.045, 1]$	$q^2/\text{GeV}^2 : [1, 6]$	$q^2/\text{GeV}^2 : [14, q^2_{\text{max}}]$
$R_{K_1(1270)}$	SM	$0.922^{+0.018}_{-0.016}$	$0.995^{+0.008}_{-0.005}$	$0.998^{+0.000}_{-0.000}$
$R_{K_1(1270)}$	S1	$0.863^{+0.069(+0.006)}_{-0.051(-0.006)}$	$0.819^{+0.048(+0.020)}_{-0.024(-0.018)}$	$0.782^{+0.003(+0.026)}_{-0.002(-0.024)}$
$R_{K_1(1270)}$	S2	$0.853^{+0.053(+0.007)}_{-0.038(-0.009)}$	$0.794^{+0.011(+0.022)}_{-0.005(-0.025)}$	$0.793^{+0.003(+0.022)}_{-0.005(-0.025)}$
$R_{K_1(1270)}$	S3	$0.860^{+0.047(+0.026)}_{-0.035(-0.026)}$	$0.805^{+0.013(+0.078)}_{-0.006(-0.078)}$	$0.802^{+0.003(+0.078)}_{-0.005(-0.078)}$
$R_{K_1(1270)}$	S4	$0.859^{+0.039(+0.026)}_{-0.029(-0.026)}$	$0.805^{+0.009(+0.078)}_{-0.011(-0.078)}$	$0.823^{+0.006(+0.095)}_{-0.009(-0.095)}$
$R_{K_1(1270)}$	S5	$0.875^{+0.044(+0.010)}_{-0.034(-0.010)}$	$0.850^{+0.019(+0.031)}_{-0.009(-0.031)}$	$0.842^{+0.002(+0.032)}_{-0.003(-0.032)}$
$R_{K_1(1270)}$	S6	$0.864^{+0.073(+0.007)}_{-0.054(-0.007)}$	$0.823^{+0.047(+0.021)}_{-0.023(-0.020)}$	$0.788^{+0.004(+0.027)}_{-0.002(-0.026)}$
$R_{K_1^L(1270)}$	SM	$0.963^{+0.103}_{-0.049}$	$0.999^{+0.014}_{-0.007}$	$0.998^{+0.000}_{-0.000}$
$R_{K_1^L(1270)}$	S1	$0.749^{+0.105(+0.026)}_{-0.050(-0.024)}$	$0.781^{+0.018(+0.028)}_{-0.008(-0.026)}$	$0.782^{+0.003(+0.026)}_{-0.002(-0.024)}$
$R_{K_1^L(1270)}$	S2	$0.773^{+0.081(+0.020)}_{-0.039(-0.023)}$	$0.793^{+0.007(+0.022)}_{-0.006(-0.025)}$	$0.794^{+0.003(+0.022)}_{-0.005(-0.025)}$
$R_{K_1^L(1270)}$	S3	$0.781^{+0.082(+0.073)}_{-0.039(-0.073)}$	$0.802^{+0.007(+0.079)}_{-0.006(-0.079)}$	$0.804^{+0.003(+0.078)}_{-0.005(-0.078)}$
$R_{K_1^L(1270)}$	S4	$0.809^{+0.084(+0.095)}_{-0.040(-0.095)}$	$0.824^{+0.007(+0.096)}_{-0.009(-0.096)}$	$0.826^{+0.006(+0.096)}_{-0.009(-0.096)}$
$R_{K_1^L(1270)}$	S5	$0.816^{+0.110(+0.030)}_{-0.053(-0.030)}$	$0.842^{+0.013(+0.032)}_{-0.007(-0.032)}$	$0.843^{+0.002(+0.032)}_{-0.003(-0.032)}$
$R_{K_1^L(1270)}$	S6	$0.754^{+0.113(+0.028)}_{-0.054(-0.026)}$	$0.788^{+0.020(+0.028)}_{-0.010(-0.026)}$	$0.789^{+0.004(+0.028)}_{-0.002(-0.026)}$
$R_{K_1^T(1270)}$	SM	$0.893^{+0.004}_{-0.003}$	$0.984^{+0.001}_{-0.000}$	$0.998^{+0.000}_{-0.000}$
$R_{K_1^T(1270)}$	S1	$0.947^{+0.005(+0.008)}_{-0.007(-0.007)}$	$0.939^{+0.067(+0.001)}_{-0.046(-0.001)}$	$0.783^{+0.003(+0.025)}_{-0.002(-0.024)}$
$R_{K_1^T(1270)}$	S2	$0.911^{+0.001(+0.004)}_{-0.001(-0.004)}$	$0.796^{+0.030(+0.024)}_{-0.017(-0.027)}$	$0.792^{+0.003(+0.022)}_{-0.005(-0.025)}$
$R_{K_1^T(1270)}$	S3	$0.910^{+0.001(+0.012)}_{-0.001(-0.012)}$	$0.814^{+0.033(+0.087)}_{-0.020(-0.087)}$	$0.801^{+0.003(+0.079)}_{-0.005(-0.079)}$
$R_{K_1^T(1270)}$	S4	$0.889^{+0.005(+0.021)}_{-0.004(-0.021)}$	$0.752^{+0.015(+0.048)}_{-0.007(-0.048)}$	$0.821^{+0.006(+0.095)}_{-0.009(-0.095)}$
$R_{K_1^T(1270)}$	S5	$0.909^{+0.001(+0.005)}_{-0.001(-0.005)}$	$0.872^{+0.028(+0.033)}_{-0.018(-0.033)}$	$0.842^{+0.002(+0.032)}_{-0.003(-0.032)}$
$R_{K_1^T(1270)}$	S6	$0.950^{+0.005(+0.008)}_{-0.007(-0.009)}$	$0.941^{+0.068(+0.002)}_{-0.047(-0.002)}$	$0.787^{+0.004(+0.027)}_{-0.002(-0.026)}$

Table 12
SM and NP predictions for the LFUV ratios $R_{K_1^{(L,T)}(1400)}$, with $\theta_{K_1} = 34^\circ$, in different bins. The first errors listed are due to the uncertainties of the form factors, and the second errors are due to the 1σ range of the best-fit Wilson coefficients in different NP scenarios.

Observable	Scenario	$q^2/\text{GeV}^2 : [0.045, 1]$	$q^2/\text{GeV}^2 : [1, 6]$	$q^2/\text{GeV}^2 : [14, q^2_{\text{max}}]$
$R_{K_1(1400)}$	SM	$0.913^{+0.011}_{-0.012}$	$0.994^{+0.006}_{-0.004}$	$0.998^{+0.000}_{-0.000}$
$R_{K_1(1400)}$	S1	$0.904^{+0.057(+0.000)}_{-0.054(-0.000)}$	$0.838^{+0.062(+0.016)}_{-0.034(-0.015)}$	$0.782^{+0.003(+0.026)}_{-0.002(-0.024)}$
$R_{K_1(1400)}$	S2	$0.873^{+0.046(+0.005)}_{-0.042(-0.006)}$	$0.792^{+0.014(+0.022)}_{-0.006(-0.025)}$	$0.793^{+0.003(+0.022)}_{-0.005(-0.025)}$
$R_{K_1(1400)}$	S3	$0.879^{+0.040(+0.018)}_{-0.037(-0.018)}$	$0.804^{+0.017(+0.079)}_{-0.008(-0.079)}$	$0.802^{+0.003(+0.078)}_{-0.005(-0.078)}$
$R_{K_1(1400)}$	S4	$0.864^{+0.034(+0.010)}_{-0.031(-0.010)}$	$0.793^{+0.013(+0.071)}_{-0.014(-0.071)}$	$0.823^{+0.006(+0.095)}_{-0.009(-0.095)}$
$R_{K_1(1400)}$	S5	$0.889^{+0.035(+0.007)}_{-0.033(-0.007)}$	$0.853^{+0.022(+0.031)}_{-0.011(-0.031)}$	$0.842^{+0.002(+0.032)}_{-0.003(-0.032)}$
$R_{K_1(1400)}$	S6	$0.906^{+0.060(+0.001)}_{-0.057(-0.001)}$	$0.842^{+0.061(+0.017)}_{-0.034(-0.016)}$	$0.788^{+0.004(+0.028)}_{-0.002(-0.026)}$
$R_{K_1^L(1400)}$	SM	$0.973^{+0.159}_{-0.067}$	$0.998^{+0.015}_{-0.007}$	$0.998^{+0.000}_{-0.000}$
$R_{K_1^L(1400)}$	S1	$0.778^{+0.192(+0.022)}_{-0.079(-0.021)}$	$0.783^{+0.022(+0.025)}_{-0.011(-0.024)}$	$0.782^{+0.003(+0.026)}_{-0.002(-0.024)}$
$R_{K_1^L(1400)}$	S2	$0.761^{+0.122(+0.023)}_{-0.049(-0.026)}$	$0.789^{+0.007(+0.022)}_{-0.007(-0.025)}$	$0.794^{+0.003(+0.022)}_{-0.005(-0.025)}$
$R_{K_1^L(1400)}$	S3	$0.770^{+0.125(+0.082)}_{-0.050(-0.082)}$	$0.798^{+0.007(+0.080)}_{-0.007(-0.080)}$	$0.803^{+0.003(+0.078)}_{-0.005(-0.078)}$
$R_{K_1^L(1400)}$	S4	$0.775^{+0.104(+0.085)}_{-0.046(-0.085)}$	$0.816^{+0.010(+0.095)}_{-0.012(-0.095)}$	$0.824^{+0.006(+0.096)}_{-0.009(-0.096)}$
$R_{K_1^L(1400)}$	S5	$0.813^{+0.163(+0.033)}_{-0.068(-0.033)}$	$0.840^{+0.013(+0.033)}_{-0.007(-0.033)}$	$0.843^{+0.002(+0.032)}_{-0.003(-0.032)}$
$R_{K_1^L(1400)}$	S6	$0.786^{+0.200(+0.024)}_{-0.083(-0.022)}$	$0.791^{+0.025(+0.027)}_{-0.012(-0.026)}$	$0.789^{+0.004(+0.028)}_{-0.002(-0.026)}$
$R_{K_1^T(1400)}$	SM	$0.893^{+0.004}_{-0.003}$	$0.984^{+0.001}_{-0.000}$	$0.997^{+0.000}_{-0.000}$
$R_{K_1^T(1400)}$	S1	$0.947^{+0.005(+0.008)}_{-0.006(-0.007)}$	$0.945^{+0.068(+0.002)}_{-0.047(-0.002)}$	$0.782^{+0.003(+0.026)}_{-0.002(-0.024)}$
$R_{K_1^T(1400)}$	S2	$0.911^{+0.001(+0.004)}_{-0.001(-0.004)}$	$0.798^{+0.031(+0.024)}_{-0.018(-0.027)}$	$0.792^{+0.003(+0.022)}_{-0.005(-0.025)}$
$R_{K_1^T(1400)}$	S3	$0.910^{+0.001(+0.012)}_{-0.001(-0.012)}$	$0.817^{+0.035(+0.087)}_{-0.021(-0.087)}$	$0.802^{+0.003(+0.079)}_{-0.005(-0.079)}$
$R_{K_1^T(1400)}$	S4	$0.890^{+0.005(+0.021)}_{-0.004(-0.021)}$	$0.753^{+0.016(+0.047)}_{-0.007(-0.047)}$	$0.822^{+0.006(+0.095)}_{-0.009(-0.095)}$
$R_{K_1^T(1400)}$	S5	$0.909^{+0.001(+0.005)}_{-0.001(-0.005)}$	$0.874^{+0.029(+0.033)}_{-0.018(-0.033)}$	$0.842^{+0.002(+0.032)}_{-0.003(-0.032)}$
$R_{K_1^T(1400)}$	S6	$0.950^{+0.005(+0.009)}_{-0.007(-0.008)}$	$0.947^{+0.069(+0.003)}_{-0.048(-0.003)}$	$0.788^{+0.004(+0.027)}_{-0.002(-0.026)}$

Table 13
SM and NP predictions for the LFUV ratios $R_{\Lambda(0,1)}$ in different bins. The first errors listed are due to the uncertainties of the form factors, and the second errors are due to the 1σ range of the best-fit Wilson coefficients in different NP scenarios.

Observable	Scenario	$q^2/\text{GeV}^2 : [0.045, 1]$	$q^2/\text{GeV}^2 : [1, 6]$	$q^2/\text{GeV}^2 : [14, q^2_{\text{max}}]$
R_Λ	SM	0.935 ± 0.024	1.001 ± 0.008	0.999 ± 0.000
R_Λ	S1	$0.896 \pm 0.038^{(+0.004)}_{(-0.004)}$	$0.838 \pm 0.024^{(+0.018)}_{(-0.016)}$	$0.785 \pm 0.001^{(+0.025)}_{(-0.024)}$
R_Λ	S2	$0.879 \pm 0.030^{(+0.006)}_{(-0.007)}$	$0.805 \pm 0.012^{(+0.021)}_{(-0.024)}$	$0.791 \pm 0.001^{(+0.022)}_{(-0.025)}$
R_Λ	S3	$0.885 \pm 0.027^{(+0.021)}_{(-0.021)}$	$0.817 \pm 0.013^{(+0.076)}_{(-0.076)}$	$0.801 \pm 0.001^{(+0.079)}_{(-0.079)}$
R_Λ	S4	$0.880 \pm 0.024^{(+0.019)}_{(-0.019)}$	$0.813 \pm 0.011^{(+0.073)}_{(-0.073)}$	$0.820 \pm 0.002^{(+0.094)}_{(-0.094)}$
R_Λ	S5	$0.899 \pm 0.027^{(+0.008)}_{(-0.008)}$	$0.863 \pm 0.013^{(+0.030)}_{(-0.030)}$	$0.842 \pm 0.001^{(+0.032)}_{(-0.032)}$
R_Λ	S6	$0.893 \pm 0.040^{(+0.004)}_{(-0.004)}$	$0.834 \pm 0.025^{(+0.019)}_{(-0.018)}$	$0.768 \pm 0.001^{(+0.029)}_{(-0.027)}$
$R_{\Lambda 0}$	SM	1.013 ± 0.088	1.004 ± 0.010	1.000 ± 0.001
$R_{\Lambda 0}$	S1	$0.805 \pm 0.082^{(+0.024)}_{(-0.023)}$	$0.790 \pm 0.010^{(+0.025)}_{(-0.023)}$	$0.784 \pm 0.001^{(+0.026)}_{(-0.024)}$
$R_{\Lambda 0}$	S2	$0.800 \pm 0.062^{(+0.023)}_{(-0.026)}$	$0.792 \pm 0.006^{(+0.022)}_{(-0.026)}$	$0.796 \pm 0.001^{(+0.022)}_{(-0.025)}$
$R_{\Lambda 0}$	S3	$0.809 \pm 0.064^{(+0.082)}_{(-0.082)}$	$0.802 \pm 0.006^{(+0.081)}_{(-0.081)}$	$0.805 \pm 0.001^{(+0.078)}_{(-0.078)}$
$R_{\Lambda 0}$	S4	$0.826 \pm 0.063^{(+0.096)}_{(-0.096)}$	$0.819 \pm 0.007^{(+0.095)}_{(-0.095)}$	$0.827 \pm 0.002^{(+0.096)}_{(-0.096)}$
$R_{\Lambda 0}$	S5	$0.860 \pm 0.084^{(+0.034)}_{(-0.034)}$	$0.845 \pm 0.008^{(+0.033)}_{(-0.033)}$	$0.845 \pm 0.001^{(+0.032)}_{(-0.032)}$
$R_{\Lambda 0}$	S6	$0.795 \pm 0.082^{(+0.026)}_{(-0.025)}$	$0.784 \pm 0.011^{(+0.027)}_{(-0.026)}$	$0.769 \pm 0.002^{(+0.029)}_{(-0.028)}$
$R_{\Lambda 1}$	SM	0.901 ± 0.004	0.987 ± 0.004	0.998 ± 0.000
$R_{\Lambda 1}$	S1	$0.936 \pm 0.007^{(+0.005)}_{(-0.005)}$	$1.064 \pm 0.081^{(+0.018)}_{(-0.016)}$	$0.786 \pm 0.001^{(+0.025)}_{(-0.023)}$
$R_{\Lambda 1}$	S2	$0.914 \pm 0.001^{(+0.002)}_{(-0.003)}$	$0.864 \pm 0.058^{(+0.022)}_{(-0.025)}$	$0.788 \pm 0.001^{(+0.022)}_{(-0.025)}$
$R_{\Lambda 1}$	S3	$0.913 \pm 0.001^{(+0.008)}_{(-0.008)}$	$0.886 \pm 0.058^{(+0.081)}_{(-0.081)}$	$0.798 \pm 0.001^{(+0.080)}_{(-0.080)}$
$R_{\Lambda 1}$	S4	$0.900 \pm 0.004^{(+0.014)}_{(-0.014)}$	$0.790 \pm 0.042^{(+0.050)}_{(-0.050)}$	$0.814 \pm 0.003^{(+0.094)}_{(-0.094)}$
$R_{\Lambda 1}$	S5	$0.912 \pm 0.001^{(+0.003)}_{(-0.003)}$	$0.927 \pm 0.040^{(+0.030)}_{(-0.030)}$	$0.840 \pm 0.001^{(+0.033)}_{(-0.033)}$
$R_{\Lambda 1}$	S6	$0.938 \pm 0.008^{(+0.006)}_{(-0.005)}$	$1.069 \pm 0.083^{(+0.020)}_{(-0.019)}$	$0.767 \pm 0.002^{(+0.029)}_{(-0.027)}$

References

[1] S. Descotes-Genon, T. Hurth, J. Matias, J. Virto, Optimizing the basis of $B \to K^* ll$ observables in the full kinematic range, J. High Energy Phys. 05 (2013) 137, arXiv:1303.5794.

[2] S. Descotes-Genon, J. Matias, J. Virto, Understanding the $B \to K^* \mu^+ \mu^-$ anomaly, Phys. Rev. D 88 (2013) 074002, arXiv:1307.5683.

[3] LHCb Collaboration, R. Aaij, et al., Measurement of form-factor-independent observables in the decay $B^0 \to K^{*0}\mu^+\mu^-$, Phys. Rev. Lett. 111 (2013) 191801, arXiv:1308.1707.

[4] LHCb Collaboration, R. Aaij, et al., Angular analysis of the $B^0 \to K^{*0}\mu^+\mu^-$ decay using 3 fb^{-1} of integrated luminosity, J. High Energy Phys. 02 (2016) 104, arXiv:1512.04442.

[5] ATLAS Collaboration, M. Aaboud, et al., Angular analysis of $B_d^0 \to K^*\mu^+\mu^-$ decays in pp collisions at $\sqrt{s} = 8$ TeV with the ATLAS detector, J. High Energy Phys. 10 (2018) 047, arXiv:1805.04000.

[6] Belle Collaboration, A. Abdesselam, et al., Angular analysis of $B^0 \to K^*(892)^0\ell^+\ell^-$, arXiv:1604.04042.

[7] Belle Collaboration, S. Wehle, et al., Lepton-flavor-dependent angular analysis of $B \to K^*\ell^+\ell^-$, Phys. Rev. Lett. 118 (11) (2017) 111801, arXiv:1612.05014.

[8] CMS Collaboration, A.M. Sirunyan, et al., Measurement of angular parameters from the decay $\mathrm{B}^0 \to \mathrm{K}^{*0}\mu^+\mu^-$ in proton-proton collisions at $\sqrt{s} = 8$ TeV, Phys. Lett. B 781 (2018) 517–541, arXiv:1710.02846.

[9] LHCb Collaboration, R. Aaij, et al., Measurement of CP-averaged observables in the $B^0 \to K^{*0}\mu^+\mu^-$ decay, Phys. Rev. Lett. 125 (1) (2020) 011802, arXiv:2003.04831.

[10] LHCb Collaboration, R. Aaij, et al., Differential branching fractions and isospin asymmetries of $B \to K^{(*)}\mu^+\mu^-$ decays, J. High Energy Phys. 06 (2014) 133, arXiv:1403.8044.

[11] LHCb Collaboration, R. Aaij, et al., Differential branching fraction and angular analysis of the decay $B^0 \to K^{*0}\mu^+\mu^-$, J. High Energy Phys. 08 (2013) 131, arXiv:1304.6325.

[12] LHCb Collaboration, R. Aaij, et al., Measurements of the S-wave fraction in $B^0 \to K^+\pi^-\mu^+\mu^-$ decays and the $B^0 \to K^*(892)^0\mu^+\mu^-$ differential branching fraction, J. High Energy Phys. 11 (2016) 047, arXiv:1606.04731, Erratum: J. High Energy Phys. 04 (2017) 142.

[13] LHCb Collaboration, R. Aaij, et al., Differential branching fraction and angular analysis of the decay $B_s^0 \to \phi\mu^+\mu^-$, J. High Energy Phys. 07 (2013) 084, arXiv:1305.2168.

[14] LHCb Collaboration, R. Aaij, et al., Angular analysis and differential branching fraction of the decay $B_s^0 \to \phi\mu^+\mu^-$, J. High Energy Phys. 09 (2015) 179, arXiv:1506.08777.

[15] W. Altmannshofer, P. Ball, A. Bharucha, A.J. Buras, D.M. Straub, M. Wick, Symmetries and asymmetries of $B \to K^*\mu^+\mu^-$ decays in the standard model and beyond, J. High Energy Phys. 01 (2009) 019, arXiv:0811.1214.

[16] C. Bobeth, G. Hiller, D. van Dyk, C. Wacker, The decay $B \to K\ell^+\ell^-$ at low hadronic recoil and model-independent $\Delta B = 1$ constraints, J. High Energy Phys. 01 (2012) 107, arXiv:1111.2558.

[17] J. Matias, F. Mescia, M. Ramon, J. Virto, Complete anatomy of $\bar{B}_d \to \bar{K}^{*0}(\to K\pi)l^+l^-$ and its angular distribution, J. High Energy Phys. 04 (2012) 104, arXiv:1202.4266.

[18] S. Descotes-Genon, J. Matias, M. Ramon, J. Virto, Implications from clean observables for the binned analysis of $B \to K^*\mu^+\mu^-$ at large recoil, J. High Energy Phys. 01 (2013) 048, arXiv:1207.2753.

[19] J. Matias, N. Serra, Symmetry relations between angular observables in $B^0 \to K^*\mu^+\mu^-$ and the LHCb P_5' anomaly, Phys. Rev. D 90 (3) (2014) 034002, arXiv:1402.6855.

[20] A. Khodjamirian, T. Mannel, A.A. Pivovarov, Y.M. Wang, Charm-loop effect in $B \to K^{(*)}\ell^+\ell^-$ and $B \to K^*\gamma$, J. High Energy Phys. 09 (2010) 089, arXiv:1006.4945.

[21] A. Khodjamirian, T. Mannel, Y.M. Wang, $B \to K\ell^+\ell^-$ decay at large hadronic recoil, J. High Energy Phys. 02 (2013) 010, arXiv:1211.0234.

[22] J. Lyon, R. Zwicky, Resonances gone topsy turvy - the charm of QCD or new physics in $b \to s\ell^+\ell^-$?, arXiv:1406.0566.

[23] S. Descotes-Genon, L. Hofer, J. Matias, J. Virto, On the impact of power corrections in the prediction of $B \to K^*\mu^+\mu^-$ observables, J. High Energy Phys. 12 (2014) 125, arXiv:1407.8526.

[24] B. Capdevila, S. Descotes-Genon, L. Hofer, J. Matias, Hadronic uncertainties in $B \to K^*\mu^+\mu^-$: a state-of-the-art analysis, J. High Energy Phys. 04 (2017) 016, arXiv:1701.08672.

[25] T. Blake, U. Egede, P. Owen, K.A. Petridis, G. Pomery, An empirical model to determine the hadronic resonance contributions to $\overline{B}^0 \to \overline{K}^{*0}\mu^+\mu^-$ transitions, Eur. Phys. J. C 78 (6) (2018) 453, arXiv:1709.03921.

[26] S. Jäger, J. Martin Camalich, On $B \to V\ell\ell$ at small dilepton invariant mass, power corrections, and new physics, J. High Energy Phys. 05 (2013) 043, arXiv:1212.2263.

[27] S. Jäger, J. Martin Camalich, Reassessing the discovery potential of the $B \to K^*\ell^+\ell^-$ decays in the large-recoil region: SM challenges and BSM opportunities, Phys. Rev. D 93 (1) (2016) 014028, arXiv:1412.3183.

[28] M. Ciuchini, M. Fedele, E. Franco, S. Mishima, A. Paul, L. Silvestrini, M. Valli, $B \to K^*\ell^+\ell^-$ decays at large recoil in the standard model: a theoretical reappraisal, J. High Energy Phys. 06 (2016) 116, arXiv:1512.07157.

[29] M. Ciuchini, M. Fedele, E. Franco, S. Mishima, A. Paul, L. Silvestrini, M. Valli, $B \to K^*\ell^+\ell^-$ in the standard model: elaborations and interpretations, in: PoS ICHEP2016, 2016, p. 584, arXiv:1611.04338.

[30] C. Bobeth, M. Chrzaszcz, D. van Dyk, J. Virto, Long-distance effects in $B \to K^*\ell\ell$ from analyticity, Eur. Phys. J. C 78 (6) (2018) 451, arXiv:1707.07305.

[31] G. Hiller, F. Kruger, More model-independent analysis of $b \to s$ processes, Phys. Rev. D 69 (2004) 074020, arXiv:hep-ph/0310219.

[32] M. Bordone, G. Isidori, A. Pattori, On the standard model predictions for R_K and R_{K^*}, Eur. Phys. J. C 76 (8) (2016) 440, arXiv:1605.07633.

[33] BELLE Collaboration, S. Choudhury, et al., Test of lepton flavor universality and search for lepton flavor violation in $B \to K\ell\ell$ decays, J. High Energy Phys. 03 (2021) 105, arXiv:1908.01848.

[34] Belle Collaboration, A. Abdesselam, et al., Test of lepton-flavor universality in $B \to K^*\ell^+\ell^-$ decays at belle, Phys. Rev. Lett. 126 (16) (2021) 161801, arXiv:1904.02440.

[35] LHCb Collaboration, R. Aaij, et al., Test of lepton universality using $B^+ \to K^+\ell^+\ell^-$ decays, Phys. Rev. Lett. 113 (2014) 151601, arXiv:1406.6482.

[36] LHCb Collaboration, R. Aaij, et al., Search for lepton-universality violation in $B^+ \to K^+\ell^+\ell^-$ decays, Phys. Rev. Lett. 122 (19) (2019) 191801, arXiv:1903.09252.

[37] LHCb Collaboration, R. Aaij, et al., Test of lepton universality in beauty-quark decays, arXiv:2103.11769.

[38] LHCb Collaboration, R. Aaij, et al., Test of lepton universality with $B^0 \to K^{*0}\ell^+\ell^-$ decays, J. High Energy Phys. 08 (2017) 055, arXiv:1705.05802.

[39] B. Capdevila, S. Descotes-Genon, J. Matias, J. Virto, Assessing lepton-flavour non-universality from $B \to K^*\ell\ell$ angular analyses, J. High Energy Phys. 10 (2016) 075, arXiv:1605.03156.

[40] LHCb Collaboration, R. Aaij, et al., Test of lepton universality with $\Lambda_b^0 \to pK^-\ell^+\ell^-$ decays, J. High Energy Phys. 05 (2020) 040, arXiv:1912.08139.

[41] LHCb Collaboration, R. Aaij, et al., Tests of lepton universality using $B^0 \to K_S^0\ell^+\ell^-$ and $B^+ \to K^{*+}\ell^+\ell^-$ decays, arXiv:2110.09501.

[42] M. Algueró, B. Capdevila, S. Descotes-Genon, J. Matias, M. Novoa-Brunet, ***b → sℓℓ*** global fits after Moriond 2021 results, in: 55th Rencontres de Moriond on QCD and High Energy Interactions, 4 2021, arXiv:2104.08921.

[43] S. Descotes-Genon, L. Hofer, J. Matias, J. Virto, Global analysis of $b \to s\ell\ell$ anomalies, J. High Energy Phys. 06 (2016) 092, arXiv:1510.04239.

[44] W. Altmannshofer, C. Niehoff, P. Stangl, D.M. Straub, Status of the $B \to K^*\mu^+\mu^-$ anomaly after Moriond 2017, Eur. Phys. J. C 77 (6) (2017) 377, arXiv:1703.09189.

[45] A.K. Alok, B. Bhattacharya, A. Datta, D. Kumar, J. Kumar, D. London, New physics in $b \to s\mu^+\mu^-$ after the measurement of R_{K^*}, Phys. Rev. D 96 (9) (2017) 095009, arXiv:1704.07397.

[46] W. Altmannshofer, P. Stangl, D.M. Straub, Interpreting hints for lepton flavor universality violation, Phys. Rev. D 96 (5) (2017) 055008, arXiv:1704.05435.

[47] L.-S. Geng, B. Grinstein, S. Jäger, J. Martin Camalich, X.-L. Ren, R.-X. Shi, Towards the discovery of new physics with lepton-universality ratios of $b \to s\ell\ell$ decays, Phys. Rev. D 96 (9) (2017) 093006, arXiv:1704.05446.

[48] M. Ciuchini, A.M. Coutinho, M. Fedele, E. Franco, A. Paul, L. Silvestrini, M. Valli, On flavourful easter eggs for new physics hunger and lepton flavour universality violation, Eur. Phys. J. C 77 (10) (2017) 688, arXiv:1704.05447.

[49] B. Capdevila, A. Crivellin, S. Descotes-Genon, J. Matias, J. Virto, Patterns of new physics in $b \to s\ell^+\ell^-$ transitions in the light of recent data, J. High Energy Phys. 01 (2018) 093, arXiv:1704.05340.

[50] M. Algueró, B. Capdevila, A. Crivellin, S. Descotes-Genon, P. Masjuan, J. Matias, M. Novoa Brunet, J. Virto, Emerging patterns of new physics with and without lepton flavour universal contributions, Eur. Phys. J. C 79 (8) (2019) 714, arXiv:1903.09578, Addendum: Eur. Phys. J. C 80 (2020) 511.

[51] A.K. Alok, A. Dighe, S. Gangal, D. Kumar, Continuing search for new physics in $b \to s\mu\mu$ decays: two operators at a time, J. High Energy Phys. 06 (2019) 089, arXiv:1903.09617.

[52] M. Ciuchini, A.M. Coutinho, M. Fedele, E. Franco, A. Paul, L. Silvestrini, M. Valli, New physics in $b \to s\ell^+\ell^-$ confronts new data on lepton universality, Eur. Phys. J. C 79 (8) (2019) 719, arXiv:1903.09632.

[53] A. Datta, J. Kumar, D. London, The B anomalies and new physics in $b \to se^+e^-$, Phys. Lett. B 797 (2019) 134858, arXiv:1903.10086.

[54] J. Aebischer, W. Altmannshofer, D. Guadagnoli, M. Reboud, P. Stangl, D.M. Straub, B-decay discrepancies after Moriond 2019, Eur. Phys. J. C 80 (3) (2020) 252, arXiv:1903.10434.

[55] K. Kowalska, D. Kumar, E.M. Sessolo, Implications for new physics in $b \to s\mu\mu$ transitions after recent measurements by Belle and LHCb, Eur. Phys. J. C 79 (10) (2019) 840, arXiv:1903.10932.

[56] A. Arbey, T. Hurth, F. Mahmoudi, D.M. Santos, S. Neshatpour, Update on the $b \to s$ anomalies, Phys. Rev. D 100 (1) (2019) 015045, arXiv:1904.08399.

[57] S. Bhattacharya, A. Biswas, S. Nandi, S.K. Patra, Exhaustive model selection in $b \to s\ell\ell$ decays: pitting cross-validation against the Akaike information criterion, Phys. Rev. D 101 (5) (2020) 055025, arXiv:1908.04835.

[58] A. Biswas, S. Nandi, S.K. Patra, I. Ray, New physics in $b \to s\ell\ell$ decays with complex Wilson coefficients, Nucl. Phys. B 969 (2021) 115479, arXiv:2004.14687.

[59] M. Algueró, B. Capdevila, S. Descotes-Genon, P. Masjuan, J. Matias, Are we overlooking lepton flavour universal new physics in $b \to s\ell\ell$?, Phys. Rev. D 99 (7) (2019) 075017, arXiv:1809.08447.

[60] S. Kumbhakar, J. Saini, New physics effects in purely leptonic B_s^* decays, Eur. Phys. J. C 79 (5) (2019) 394, arXiv:1807.04055.

[61] A.K. Alok, S. Kumbhakar, S. Uma Sankar, A unique discrimination between new physics scenarios in $b \to s\mu^+\mu^-$ anomalies, arXiv:2001.04395.

[62] G. Hiller, M. Schmaltz, Diagnosing lepton-nonuniversality in $b \to s\ell\ell$, J. High Energy Phys. 02 (2015) 055, arXiv:1411.4773.

[63] W. Wang, S. Zhao, Implications of the R_K and R_{K^*} anomalies, Chin. Phys. C 42 (1) (2018) 013105, arXiv:1704.08168.

[64] Z.-R. Huang, M.A. Paracha, I. Ahmed, C.-D. Lü, Testing leptoquark and Z' models via $B \to K_1(1270, 1400)\mu^+\mu^-$ decays, Phys. Rev. D 100 (5) (2019) 055038, arXiv:1812.03491.

[65] R. Dutta, Model independent analysis of new physics effects on $B_c \to (D_s,\, D_s^*)\,\mu^+\mu^-$ decay observables, Phys. Rev. D 100 (7) (2019) 075025, arXiv:1906.02412.

[66] R. Alonso, P. Cox, C. Han, T.T. Yanagida, Anomaly-free local horizontal symmetry and anomaly-full rare B-decays, Phys. Rev. D 96 (7) (2017), arXiv:1704.08158.

[67] R. Alonso, P. Cox, C. Han, T.T. Yanagida, Flavoured $B - L$ local symmetry and anomalous rare B decays, Phys. Lett. B 774 (2017) 643–648, arXiv:1705.03858.

[68] G.H. Duan, X. Fan, M. Frank, C. Han, J.M. Yang, A minimal $U(1)'$ extension of MSSM in light of the B decay anomaly, Phys. Lett. B 789 (2019) 54–58, arXiv:1808.04116.

[69] C. Bobeth, M. Misiak, J. Urban, Photonic penguins at two loops and m_t dependence of $BR[B \to X_s l^+ l^-]$, Nucl. Phys. B 574 (2000) 291–330, arXiv:hep-ph/9910220.

[70] M. Beneke, T. Feldmann, D. Seidel, Systematic approach to exclusive $B \to V l^+ l^-$, $V\gamma$ decays, Nucl. Phys. B 612 (2001) 25–58, arXiv:hep-ph/0106067.

[71] H.H. Asatrian, H.M. Asatrian, C. Greub, M. Walker, Two loop virtual corrections to $B \to X_s l^+ l^-$ in the standard model, Phys. Lett. B 507 (2001) 162–172, arXiv:hep-ph/0103087.

[72] H.H. Asatryan, H.M. Asatrian, C. Greub, M. Walker, Calculation of two loop virtual corrections to $b \to s l^+ l^-$ in the standard model, Phys. Rev. D 65 (2002) 074004, arXiv:hep-ph/0109140.

[73] C. Greub, V. Pilipp, C. Schupbach, Analytic calculation of two-loop QCD corrections to $b \to s l^+ l^-$ in the high q^2 region, J. High Energy Phys. 12 (2008) 040, arXiv:0810.4077.

[74] D. Du, A.X. El-Khadra, S. Gottlieb, A.S. Kronfeld, J. Laiho, E. Lunghi, R.S. Van de Water, R. Zhou, Phenomenology of semileptonic B-meson decays with form factors from lattice QCD, Phys. Rev. D 93 (3) (2016) 034005, arXiv:1510.02349.

[75] P. Colangelo, F. De Fazio, W. Wang, $B_s \to f_0(980)$ form factors and B_s decays into $f_0(980)$, Phys. Rev. D 81 (2010) 074001, arXiv:1002.2880.

[76] T. Aliev, K. Azizi, M. Savci, Analysis of rare $B \to K_0^*(1430)\ell^+\ell^-$ decay within QCD sum rules, Phys. Rev. D 76 (2007) 074017, arXiv:0710.1508.

[77] C.-D. Lü, Y.-L. Shen, Y.-M. Wang, Y.-B. Wei, QCD calculations of $B \to \pi, K$ form factors with higher-twist corrections, J. High Energy Phys. 01 (2019) 024, arXiv:1810.00819.

[78] C. Bourrely, I. Caprini, L. Lellouch, Model-independent description of $B \to \pi l \nu$ decays and a determination of $|V_{ub}|$, Phys. Rev. D 79 (2009) 013008, arXiv:0807.2722, Erratum: Phys. Rev. D 82 (2010) 099902.

[79] A. Bharucha, D.M. Straub, R. Zwicky, $B \to V\ell^+\ell^-$ in the standard model from light-cone sum rules, J. High Energy Phys. 08 (2016) 098, arXiv:1503.05534.

[80] H. Hatanaka, K.-C. Yang, $K_1(1270) - K_1(1400)$ mixing angle and new-physics effects in $B \to K_1 l^+ l^-$ decays, Phys. Rev. D 78 (2008) 074007, arXiv:0808.3731.

[81] S. Ishaq, F. Munir, I. Ahmed, Lepton polarization asymmetries in $B \to K_1 l^+ l^-$ decay as a searching tool for new physics, J. High Energy Phys. 07 (2013) 006.

[82] F. Munir, S. Ishaq, I. Ahmed, Polarized forward-backward asymmetries of lepton pair in $B \to K_1 \ell^+ \ell^-$ decay in the presence of new physics, PTEP 2016 (1) (2016) 013B02, arXiv:1511.07075.

[83] W. Detmold, S. Meinel, $\Lambda_b \to \Lambda \ell^+ \ell^-$ form factors, differential branching fraction, and angular observables from lattice QCD with relativistic b quarks, Phys. Rev. D 93 (7) (2016) 074501, arXiv:1602.01399.

[84] A. Faessler, T. Gutsche, M.A. Ivanov, J.G. Korner, V.E. Lyubovitskij, The exclusive rare decays $B \to$ K(K*) $\bar{\ell}\ell$ and $B_c \to$ D(D*) $\bar{\ell}\ell$ in a relativistic quark model, Eur. Phys. J. Direct 4 (1) (2002) 18, arXiv:hep-ph/0205287.

[85] J. Gratrex, M. Hopfer, R. Zwicky, Generalised helicity formalism, higher moments and the $B \to K_{J_K}(\to K\pi)\bar{\ell}_1\ell_2$ angular distributions, Phys. Rev. D 93 (5) (2016) 054008, arXiv:1506.03970.

[86] D. Ebert, R. Faustov, V. Galkin, Rare semileptonic decays of B and B_c mesons in the relativistic quark model, Phys. Rev. D 82 (2010) 034032, arXiv:1006.4231.

[87] T. Gutsche, M.A. Ivanov, J.G. Korner, V.E. Lyubovitskij, P. Santorelli, Rare baryon decays $\Lambda_b \to \Lambda l^+ l^- (l = e, \mu, \tau)$ and $\Lambda_b \to \Lambda\gamma$: differential and total rates, lepton- and hadron-side forward-backward asymmetries, Phys. Rev. D 87 (2013) 074031, arXiv:1301.3737.

[88] F. James, M. Roos, Minuit: a system for function minimization and analysis of the parameter errors and correlations, Comput. Phys. Commun. 10 (1975) 343–367.

[89] D.M. Straub, flavio: a Python package for flavour and precision phenomenology in the Standard Model and beyond, arXiv:1810.08132.

[90] J. Aebischer, J. Kumar, D.M. Straub, Wilson: a Python package for the running and matching of Wilson coefficients above and below the electroweak scale, Eur. Phys. J. C 78 (12) (2018) 1026, arXiv:1804.05033.

[91] LHCb Collaboration, S. Ferreres-Solé, The beauty of the rare: $B_{(s)} \to \mu^+\mu^-$ at the LHCb, in: 55th Rencontres de Moriond on Electroweak Interactions and Unified Theories, 6 2021, arXiv:2106.15995.

[92] LHCb Collaboration, R. Aaij, et al., Angular analysis of the $B^+ \to K^{*+}\mu^+\mu^-$ decay, Phys. Rev. Lett. 126 (16) (2021) 161802, arXiv:2012.13241.

[93] CMS Collaboration, A.M. Sirunyan, et al., Angular analysis of the decay $\mathrm{B}^+ \to \mathrm{K}^+\mu^+\mu^-$ in proton-proton collisions at $\sqrt{s} = 8$ TeV, Phys. Rev. D 98 (11) (2018) 112011, arXiv:1806.00636.

[94] LHCb Collaboration, R. Aaij, et al., Strong constraints on the $b \to s\gamma$ photon polarisation from $B^0 \to K^{*0}e^+e^-$ decays, J. High Energy Phys. 12 (2020) 081, arXiv:2010.06011.

[95] N. Gubernari, A. Kokulu, D. van Dyk, $B \to P$ and $B \to V$ form factors from B-meson light-cone sum rules beyond leading twist, J. High Energy Phys. 01 (2019) 150, arXiv:1811.00983.

[96] A. Crivellin, C. Greub, D. Müller, F. Saturnino, Importance of loop effects in explaining the accumulated evidence for new physics in B decays with a vector leptoquark, Phys. Rev. Lett. 122 (1) (2019) 011805, arXiv:1807.02068.

[97] C. Bobeth, A.J. Buras, A. Celis, M. Jung, Patterns of flavour violation in models with vector-like quarks, J. High Energy Phys. 04 (2017) 079, arXiv:1609.04783.

[98] J. Kumar, D. London, New physics in $b \to se^+e^-$?, Phys. Rev. D 99 (7) (2019) 073008, arXiv:1901.04516.

[99] Belle-II Collaboration, W. Altmannshofer, et al., The Belle II physics book, PTEP 2019 (12) (2019) 123C01, arXiv:1808.10567, Erratum: PTEP 2020 (2020) 029201.

[100] H. Hatanaka, K.-C. Yang, $B \to K_1\gamma$ decays in the light-cone QCD sum rules, Phys. Rev. D 77 (2008) 094023, arXiv:0804.3198, Erratum: Phys. Rev. D 78 (2008) 059902.

[101] H.-Y. Cheng, Revisiting axial-vector meson mixing, Phys. Lett. B 707 (2012) 116–120, arXiv:1110.2249.

[102] Particle Data Group Collaboration, M. Tanabashi, et al., Review of particle physics, Phys. Rev. D 98 (3) (2018) 030001.

[103] K. Hayasaka, Z. Huang, E. Kou, The hadronic τ decay $\tau^- \to K_1^-\nu_\tau \to (K^-\omega)\nu_\tau \to (K^-\pi^+\pi^-\pi^0)\nu_\tau$ and the axial vector mixing angle, Eur. Phys. J. C 81 (2021) 502, arXiv:2102.00752.

[104] LHCb Collaboration, R. Aaij, et al., Physics case for an LHCb upgrade II - opportunities in flavour physics, and beyond, in the HL-LHC era, arXiv:1808.08865.

[105] Particle Data Group Collaboration, P. Zyla, et al., Review of particle physics, PTEP 2020 (8) (2020) 083C01.

[106] A. Ali, A.Y. Parkhomenko, A.V. Rusov, Precise calculation of the dilepton invariant-mass spectrum and the decay rate in $B^\pm \to \pi^\pm\mu^+\mu^-$ in the SM, Phys. Rev. D 89 (9) (2014) 094021, arXiv:1312.2523.

[107] K.-C. Yang, Light-cone distribution amplitudes of axial-vector mesons, Nucl. Phys. B 776 (2007) 187–257, arXiv:0705.0692.

[108] P. Böer, T. Feldmann, D. van Dyk, Angular analysis of the decay $\Lambda_b \to \Lambda(\to N\pi)\ell^+\ell^-$, J. High Energy Phys. 01 (2015) 155, arXiv:1410.2115.

[109] H.E. Haber, Spin formalism and applications to new physics searches, in: The Proceedings of 21st Annual SLAC Summer Institute on Particle Physics: Spin Structure in High-Energy Processes, 1993, pp. 231–272, arXiv:hep-ph/9405376.